



**HAL**  
open science

## **Lis1 mutation prevents basal radial glia-like cell production in the mouse**

Maxime Penisson, Mingyue Jin, Shengming Wang, Shinji Hirotsune, Fiona Francis, Richard Belvindrah

► **To cite this version:**

Maxime Penisson, Mingyue Jin, Shengming Wang, Shinji Hirotsune, Fiona Francis, et al.. Lis1 mutation prevents basal radial glia-like cell production in the mouse. Human Molecular Genetics, 2021, 10.1093/hmg/ddab295 . hal-03379982

**HAL Id: hal-03379982**

**<https://hal.sorbonne-universite.fr/hal-03379982>**

Submitted on 15 Oct 2021

**HAL** is a multi-disciplinary open access archive for the deposit and dissemination of scientific research documents, whether they are published or not. The documents may come from teaching and research institutions in France or abroad, or from public or private research centers.

L'archive ouverte pluridisciplinaire **HAL**, est destinée au dépôt et à la diffusion de documents scientifiques de niveau recherche, publiés ou non, émanant des établissements d'enseignement et de recherche français ou étrangers, des laboratoires publics ou privés.

1 **Lis1 mutation prevents basal radial glia-like cell production in the mouse**

2

3 Maxime Penisson <sup>1,2,3</sup>, Mingyue Jin <sup>4¶</sup>, Shengming Wang <sup>4</sup>, Shinji Hirotsune <sup>4</sup>, Fiona Francis\*

4 <sup>1,2,3,#</sup>, Richard Belvindrah <sup>1,2,3,#</sup>

5

6

7

8 1. INSERM U 1270, Paris, France

9 2. Sorbonne University, UMR-S 1270, F-75005 Paris, France

10 3. Institut du Fer à Moulin, Paris, France.

11 4. Osaka City University Graduate School of Medicine, Genetic Disease Research

12 Asahi-machi 1-4-3, Osaka, JP 545-8585

13

14

15

16

17

18

19 <sup>#</sup>These authors contributed equally.

20 <sup>¶</sup>Present address: Guangxi Key Laboratory of Brain and Cognitive Neuroscience, Guilin

21 Medical University, No.1. Zhiyuan Road, Lingui, Guilin, 541199, Guangxi, China

22

23 \*Corresponding author: Fiona Francis, Institut du Fer à Moulin, 17 rue du Fer à Moulin,

24 75005 Paris France. Tel: +33145876145 Email: fiona.francis@inserm.fr

25

26

27

28 **Abstract**

29 Human cerebral cortical malformations are associated with progenitor proliferation and neuronal  
30 migration abnormalities. Progenitor cells include apical radial glia, intermediate progenitors and basal  
31 (or outer) radial glia (bRGs or oRGs). bRGs are few in number in lissencephalic species (e.g. the  
32 mouse) but abundant in gyrencephalic brains. The *LIS1* gene coding for a dynein regulator, is mutated  
33 in human lissencephaly, associated also in some cases with microcephaly. LIS1 was shown to be  
34 important during cell division and neuronal migration. Here, we generated bRG-like cells in the mouse  
35 embryonic brain, investigating the role of Lis1 in their formation. This was achieved by *in utero*  
36 electroporation of a hominoid-specific gene *TBC1D3* (coding for a RAB-GAP protein) at mouse  
37 embryonic day (E) 14.5. We first confirmed that *TBC1D3* expression in wild-type (WT) brain  
38 generates numerous Pax6<sup>+</sup> bRG-like cells that are basally localized. Second, using the same approach,  
39 we assessed the formation of these cells in heterozygote *Lis1* mutant brains. Our novel results show  
40 that *Lis1* depletion in the forebrain from E9.5 prevented subsequent *TBC1D3*-induced bRG-like cell  
41 amplification. Indeed, we observe perturbation of the ventricular zone (VZ) in the mutant. *Lis1*  
42 depletion altered adhesion proteins and mitotic spindle orientations at the ventricular surface and  
43 increased the proportion of abventricular mitoses. Progenitor outcome could not be further altered by  
44 *TBC1D3*. We conclude that disruption of *Lis1*/LIS1 dosage is likely to be detrimental for appropriate  
45 progenitor number and position, contributing to lissencephaly pathogenesis.

46

## 47 Introduction

48

49 The development of the cerebral cortex relies on different types of progenitor cell situated in a  
50 neuroepithelium adjacent to the cerebral ventricles. These cells produce neurons which *in fine* will  
51 form networks that underlie brain functions (Taverna et al., 2014). Early neuroepithelial cells give rise  
52 to apical radial glia cells (aRGs) which are localized in the ventricular zone (VZ) and possess a short  
53 apical process descending to the ventricle and a long basal process extending to the pial surface (Götz  
54 and Huttner, 2005). These progenitor cells proliferate producing either immature glutamatergic  
55 neurons which will migrate along aRG basal fibers in the intermediate zone (IZ) to reach their final  
56 position in the cortical plate (CP), or other subpopulations of progenitors: e.g. intermediate progenitors  
57 (IPs) and basal radial glial cells (bRGs). IPs are multipolar cells that are localized mainly in the  
58 subventricular zone (SVZ) and can produce deep and upper layer neurons (Agirman et al., 2017;  
59 Hevner, 2019). bRGs are rare in the rodent, but abundant in gyrencephalic species where they are  
60 localized in an outer SVZ (OSVZ) and inner SVZ (ISVZ). In these species, they have been shown to  
61 play a major role during cortical development (Fietz et al., 2010; Hansen et al., 2010; Reillo et al.,  
62 2011; Wang et al., 2011; Florio et al., 2015; Penisson et al., 2019). They are highly proliferative cells  
63 and can produce neurons and IPs, but unlike rodent IPs, they have the ability to self-renew  
64 extensively, therefore constituting a renewed pool of progenitors for cortical development (Hansen et  
65 al., 2010; LaMonica et al., 2012; Betizeau et al., 2013; Martínez-Martínez et al., 2016). Basal RGs  
66 present different morphologies, classically they were described with only a basal process, but they can  
67 also have only an apical process or both (Betizeau et al., 2013; Pilz et al., 2013). It is important to  
68 assess how perturbation of bRG function may contribute to the apparition of cortical disorders.

69 Malformations of cortical development (MCDs) are rare pathologies characterized by intellectual  
70 disability and/or epilepsy. They are associated with abnormalities in cortical structure and/or the  
71 number of neurons (Desikan and Barkovich, 2016). Linked to genetic mutations or environmental  
72 factors (Romero et al., 2018), they have been associated with defects in cell proliferation and/or

73 neuronal migration, and include micro- or macrocephaly (reduction or enlargement of cerebral volume  
74 respectively), lissencephaly (absence of or abnormal folds) or heterotopias (presence of grey matter  
75 within the white matter) (Barkovich et al., 2012; Capuano et al., 2017; Subramanian et al., 2020).

76 *LIS1*, coding for a regulator of dynein activity, was the first gene to be linked with a neuronal  
77 migration disorder: the Miller-Dieker syndrome (MDS) (Dobyns et al., 1993; Reiner and Sapir, 2013,  
78 Cianfrocco et al., 2015). MDS is characterized by lissencephaly and facial abnormalities and is caused  
79 by a contiguous deletion of genes on the short arm of chromosome 17. While several genes are deleted  
80 in MDS, *LIS1* appears to be one of the main actors in this pathology, as heterozygous intragenic  
81 deletions and point mutations also lead to lissencephaly, with varying degrees of severity, including  
82 microcephaly (Lo Nigro et al., 1997; Yingling et al., 2003).

83 In the naturally lissencephalic mouse, *Lis1* haploinsufficiency leads to mild neocortical and  
84 hippocampal disorganization, contrasting with the extremely severe human disorder. Only further  
85 depletion of *Lis1* to approximately 35 % of normal, induced a severe neocortical phenotype (Hirotsume  
86 et al., 1998; Gambello et al., 2003). Reduced *Lis1* dosage was shown to affect neuronal migration  
87 (Tsai et al., 2005), as well as mitotic spindle orientation in neuroepithelial cells and aRGs (Yingling et  
88 al., 2008). This leads to a depletion of the progenitor pool, by increased cell cycle exit of aRGs  
89 transiently favorising neurogenesis (Pramparo et al., 2010; Iefremova et al., 2017). Human MDS  
90 organoids were produced (Bershteyn et al., 2017; Iefremova et al., 2017) revealing, as well as other  
91 defects, bRGs with longer mitoses and altered mitotic somal translocation (Bershteyn et al., 2017).  
92 However, the specific role of LIS1 in bRG generation still remains poorly understood, as well as more  
93 generally the involvement of bRGs in the pathogenesis of lissencephaly. There is indeed a strong need  
94 to revisit MCD pathogenesis, considering the more recently identified bRGs, questioning how  
95 perturbation of their function might contribute to these disorders.

96 Various genes and mechanisms have been described in the past decade to regulate bRG production  
97 and amplification (Penisson et al., 2019). Several models exist to study these cells in different  
98 organisms. Certain reports in the mouse brain have described an artificial enrichment of cells having  
99 many characteristic features of bRGs, i.e. localized in basal positions, with basal and/or apical

100 processes, expressing markers such as Pax6, Sox2, phospho-Vimentin, and with the ability to self-  
101 amplify or produce neurons (Stahl et al., 2013; Lui et al., 2014; Florio et al., 2015; Wong et al., 2015;  
102 Ju et al., 2016; Heng et al., 2017; Liu et al., 2017; Tavano et al., 2018). We have termed these ‘bRG-  
103 like cells’, because they share many molecular and morphological features with human and primate  
104 bRGs, and their amplification sometimes even leads to the formation of folds on the surface of the  
105 mouse brain (Stahl et al., 2013; Ju et al., 2016; Liu et al., 2017). Hence, with the aim of studying the  
106 role of Lis1 in the genesis and function of bRGs, we set out to combine the study of a floxed mouse  
107 line for *Lis1* (Hirotsune et al., 1998) with an amplification of bRG-like cells. We selected to use  
108 *TBC1D3*, a hominoid-specific RAB-GAP, known to favorize the generation of bRG-like cells upon  
109 expression in the mouse brain through increased delamination of progenitors from the VZ to more  
110 basal regions and increased proliferation of basal progenitors (Ju et al., 2016).

111 In this study, we confirmed that *TBC1D3* expression in the mouse via *in utero* electroporation (IUE) at  
112 E14.5 promotes the generation of bRG-like cells 2 days later. We found that an early heterozygote  
113 depletion of *Lis1* at E9.5 using the *Emx1-Cre* mouse line (Gorski et al., 2002) prevents the *TBC1D3*-  
114 dependent bRG-like cell amplification which occurs in control animals. Indeed, baseline modifications  
115 already appear to exist in *Lis1* mutant developing brains and no further additive effects are generated  
116 by *TBC1D3* expression. It is likely that early *Lis1* depletion by 50%, while not inducing heavily  
117 deleterious effects, generates sufficient cellular modifications to prevent *TBC1D3* from generating  
118 bRG-like cells. Thus, *Lis1* is necessary for the production of murine bRG-like cells, associated with  
119 expression of a hominoid-specific gene which contributes to bRG generation in humans.

120

## 121 Results

122

### 123 ***TBC1D3* promotes the generation of bRG-like cells in the mouse**

124

125 The bRG population is naturally scarce in the developing mouse brain, we therefore expressed  
126 *TBC1D3* to amplify this population (Ju et al., 2016). To test this tool under our experimental  
127 conditions, WT mice were first electroporated at E14.5 with pCS2-cMyc-*TBC1D3* (Ju et al, 2016)  
128 together with a pCAG-IRES-tdTomato plasmid to identify electroporated cells, compared to pCAG-  
129 IRES-tdTomato alone (Figure 1A-B'). Mice were sacrificed two days later. First, we checked the  
130 efficiency of co-electroporation with both plasmids by quantifying the percentage of double labeled  
131 tdTomato-positive (+) cMyc-positive (+) cells (Supplementary Figure 1). We found that the vast  
132 majority (87.54%) of electroporated cells co-express tdTomato and c-Myc showing high efficiency of  
133 the co-electroporation method. *TBC1D3* expression led to the presence of tdTomato-positive (+)  
134 basally-positioned cells with somata localized in the SVZ and IZ (Figure 1B'). These cells possessed  
135 either a basal process or both an apical and basal process, as described previously for bRG cells  
136 (Betizeau et al., 2013). Immunohistochemistry showed that many basal cells with bRG-like  
137 morphology were Pax6+ (Figure 1B', B''), as also previously shown by Ju et al., 2016.  
138 Quantifications showed a significant increase in the proportion of Pax6+ cells among electroporated  
139 cells when *TBC1D3* is expressed compared to control. This includes when considering the entire  
140 cortical wall (Total, 10.9%  $\pm$  1.9 for control versus (vs.) 24.5%  $\pm$  0.1 for *TBC1D3*, p<0.01), as well as  
141 when dividing the cortical wall into the VZ (36.9%  $\pm$  3.5 for control vs. 49.9%  $\pm$  7.7 for *TBC1D3*,  
142 p<0.01), SVZ (5.5%  $\pm$  0.9 for control vs. 15.1%  $\pm$  4.5 for *TBC1D3*, p<0.05) and IZ (1.9%  $\pm$  0.5 for  
143 control vs. 11.8%  $\pm$  2.6 for *TBC1D3*, p<0.05) (Figure 1C). Overall, this suggests that *TBC1D3*  
144 expression increases numbers of Pax6+ RG, some of which leave the VZ and move towards more  
145 basal regions, potentially by apical delamination or during mitosis by a shift to more oblique and/or  
146 horizontal divisions not allowing apical adhesion (Shitamukai et al., 2011).

147

148 The effect of *TBC1D3* expression on mitoses was first assessed by performing phospho-Histone 3  
149 (PH3) immunostaining (Figure 1D, D'). *TBC1D3* expression led to increased numbers of PH3+  
150 mitotic cells compared to the control plasmid. This was significant when considering the proportion of  
151 mitotic cells amongst fluorescent cells across the whole cortical wall (4.5%  $\pm$  0.2 for control vs. 10.8%

152  $\pm 1.1$  for TBC1D3,  $p < 0.01$ ), as well as specifically when assessing the VZ ( $12.6\% \pm 0.5$  for control vs.  
153  $20.8\% \pm 3.4$  for TBC1D3,  $p < 0.001$ ) (Figure 1E) and tendencies were also observed in the SVZ ( $2.38\%$   
154  $\pm 0.81$  for control vs.  $6.13\% \pm 3.16$  for TBC1D3) and IZ ( $0.81\% \pm 0.52$  for control vs.  $2.50\% \pm 2.4$  for  
155 TBC1D3). aRG mitoses generally take place at the ventricular surface in the control condition (Figure  
156 1D), related to interkinetic nuclear migration (Kulikova et al., 2011; Taverna et al., 2014). When  
157 TBC1D3 was expressed, the location of mitoses displayed a notable basal shift. We quantified the  
158 proportion of these abventricular mitoses *i.e.* all dividing cells in the VZ, SVZ and IZ with nuclei that  
159 do not contact the ventricular surface. Indeed, the proportion of abventricular mitoses increased (Total:  
160  $43.0\% \pm 11.0$  for control vs.  $69.1\% \pm 1.5$  for TBC1D3,  $p = 0.052$ , data not shown), with a decreased  
161 proportion of divisions at the ventricular surface. Considering only abventricular mitoses in the VZ  
162 (Figure 1F), there were  $25.6\% \pm 11.2$  for control vs.  $57.5\% \pm 8.2$  for TBC1D3,  $p < 0.01$ ) (Figure 1F).  
163 The latter suggests that basal mitoses were more likely to occur in the presence of TBC1D3. Overall,  
164 these results are consistent with the original study (Ju et al, 2016) suggesting that TBC1D3 expression  
165 in mouse brain progenitors promotes the generation of bRG-like cells.

166

### 167 **Forebrain-specific *Lis1* knockout severely perturbs cortical development**

168

169 After validating the production of TBC1D3-induced bRG-like cells, *Lis1* mutants were generated.  
170 Various Cre lines have been used in the past to induce *Lis1*<sup>fl/fl</sup> recombination, showing defects  
171 depending on the timing of *Lis1* depletion, targeted cell types and the dosage of the *Lis1* remaining  
172 (Hirotsume et al., 1998; Gambello et al., 2003; Yingling et al., 2008). We set out to deplete *Lis1* in a  
173 forebrain-specific manner at an early stage, before the onset of neurogenesis, to ensure depletion of  
174 this gene in all neural progenitors. We used a new *Lis1*<sup>fl/fl</sup> stock from which the neo-cassette had been  
175 removed (referred to here as *Lis1*<sup>fl/fl</sup>). Indeed, the presence of the neo-cassette was previously shown to  
176 alter *Lis1* gene expression (Hirotsume et al., 1998; Gambello et al., 2003), generating *de facto* an  
177 hypomorphic allele even in the absence of the Cre recombinase. To deplete *Lis1* in neo-removed  
178 *Lis1*<sup>fl/fl</sup> mice, an *Emx1*-IRES-Cre knockin mouse was used (referred to here as *Emx1*-Cre) to induce



179 recombination in neural progenitors starting at E9.5 (Gorski et al., 2002). To verify the pattern of  
180 expression of the Cre, Emx1-Cre animals were crossed with the Rosa26-EGFP<sup>RCE/RCE</sup> line (Sousa et  
181 al., 2009). Brains of the embryos showed GFP expression restricted to the cortex, as well as in fiber  
182 tracts including the corpus callosum and the anterior commissure (Supplementary Figure 2). No  
183 expression was observed in the sub-pallium.

184 After having confirmed the recombination pattern in the Emx1-Cre mouse line, *Lis1*<sup>fl/fl</sup> animals were  
185 crossed with Emx1-Cre animals, to obtain *Lis1*<sup>fl/+</sup> Emx1-Cre<sup>+Cre</sup> mutant mice. These were then crossed  
186 with *Lis1*<sup>fl/fl</sup> mice to obtain WT (*Lis1*<sup>fl/+</sup> or *Lis1*<sup>fl/fl</sup>; Emx1-Cre<sup>+Cre</sup>), heterozygote (HET, *Lis1*<sup>fl/+</sup>; Emx1-  
187 Cre<sup>+Cre</sup>) and knockout (KO, *Lis1*<sup>fl/fl</sup>; Emx1-Cre<sup>+Cre</sup>) animals in the same litter (Figure 2A). Postnatal  
188 day 0 (P0) brains of HET pups did not show any macroscopic cortical differences when compared to  
189 control, consistent with previous studies (Hirotsume et al., 1998; Gambello et al., 2003). However,  
190 brains of KO animals were largely devoid of a cortex (Figure 2B, D). This phenotype was easily  
191 visible at E14.5 (data not shown), and KO animals died between P3 and P7. This result further  
192 confirmed that reducing the dosage of *Lis1* by half does not have obvious major deleterious effects on  
193 mouse cortical development (and HETs survive normally), whereas further decrease has severe  
194 consequences (Hirotsume et al., 1998; Gambello et al., 2003).

195 Considering that the cortex is almost totally absent in KO animals, making a fine assessment of *Lis1*  
196 function in KO progenitors less appropriate, we continued our experiments comparing only WT and  
197 HET animals. To that end, *Lis1*<sup>fl/fl</sup> mice were crossed with Emx1-Cre<sup>+Cre</sup> animals to obtain WT (Cre  
198 negative) or HET embryos in the same litter. To evaluate whether *Lis1* depletion by 50% had an  
199 impact on cortical organization, even though no major defects were observed macroscopically, *Tbr1*  
200 immunostaining was performed. No significant differences were observed between WT and HET mice  
201 when assessing the number of *Tbr1*<sup>+</sup> deep layer neurons (Figure 2 C, E). This together with the  
202 cortical thickness measurements suggests that in the HET state, cortical neuron production and  
203 migration occur relatively normally.

204 Performing the same crosses and generating pregnant females, embryos were then electroporated at  
205 E14.5 with pCS2-cMyc-TBC1D3 or control (pCS2-cMyc) plasmid together with the pCAG-IRES-

206 tdTomato reporter plasmid, and mice were sacrificed 2 days later. Activated caspase 3 (aCas3)  
207 immunostaining was first performed to assess cell death. No significant differences were observed,  
208 when depleting *Lis1*, or expressing TBC1D3 (Supplementary Figure 3A, B).

209 Overall, these results with early forebrain inactivation of *Lis1* showed that full KO at E9.5 leads to  
210 severe cortical developmental defects, while depletion of *Lis1* by 50% has no obvious effect on  
211 cortical layering organization and a non-significant impact on cell death.

212

### 213 **Lis1 depletion prevents bRG-like cell amplification upon TBC1D3 expression**

214

215 We next investigated whether, in the presence of TBC1D3, *Lis1* depletion would alter or prevent the  
216 generation of bRG-like cells. To evaluate the effect of TBC1D3 (or the control plasmid) expression on  
217 RGs in the *Lis1* mutant cortex, Pax6 and Ki67 co-immunostaining was performed (Figure 3A-E',  
218 Supplementary Figure 4 for higher magnifications). Pax6+ tdTomato+ cells were assessed across the  
219 cortical wall and in the different zones (Figure 3F). Under these conditions, no significant differences  
220 in the percentages of Pax6+ cells within the tdTomato population were observed in the VZ and SVZ  
221 regions. The overall percentage of Pax6+ cells amongst the tdTomato+ cells across the cortical wall  
222 also did not show significant differences, although there was a tendency for increase in the TBC1D3  
223 WT condition. In the IZ, no differences were noted between WT and HET brains electroporated with  
224 the control plasmid, however a significant increase in the proportion of Pax6+ tdTomato+ cells was  
225 observed when TBC1D3 was expressed in WT brains (9.0% ± 3.0 for Control WT vs. 33.2% ± 9.4 for  
226 TBC1D3 WT, p<0.05). However, when TBC1D3 is expressed in HET brains, numbers of Pax6+ cells  
227 were similar in the IZ to that of the HET condition electroporated with the control plasmid (7.8% ± 6.5  
228 for Control HET vs. 13.3% ± 3.0 for TBC1D3 HET, no significant differences). This suggests that  
229 *Lis1* depletion largely prevents bRG-like cell amplification in the presence of TBC1D3.

230 The effect of *Lis1* depletion on cycling RGs was then assessed by quantifying the proportion of cells  
231 co-labeled with Pax6 and Ki67, a marker of proliferation (Figure 3G, H). Overall proportions of Ki67+

232 cells did not differ significantly between the genotypes and conditions, nor did positions of Pax6+  
233 Ki67+ cells in non-electroporated HET brains (Figure 3G, Supplementary Figure 5). However, after  
234 electroporation with TBC1D3, when considering Pax6+ Ki67+ tdTomato+ triple labeled cells (Figure  
235 3H), similar results to those described in Figure 3F were obtained: in the IZ no difference was found  
236 between WT and HET conditions with the control plasmid, however TBC1D3 expression in WT  
237 animals resulted in an increased proportion of Pax6+ Ki67+ cells ( $4.2\% \pm 1.5$  for Control WT vs.  
238  $16.7\% \pm 4.1$  for TBC1D3 WT,  $p < 0.05$ ) as shown previously by Ju et al. (2016) with Pax6 staining.  
239 This increase was not observed with Lis1 depletion ( $4.7\% \pm 1.2$  for TBC1D3 HET vs.  $16.7\% \pm 4.1$  for  
240 TBC1D3 WT vs,  $p < 0.05$ ). This suggests that TBC1D3 expression in WT induces an increased  
241 production of cycling bRG-like Pax6+ cells in the IZ, and importantly, Lis1 depletion prevents this  
242 phenomenon from occurring.

243 To assess whether Lis1 dosage also influences the ability of Pax6+ RGs to cycle, we measured the  
244 proportion of cycling RGs (Pax6+ Ki67+ tdTomato+) among electroporated RGs (Pax6+ tdTomato+)  
245 (Figure 3I). No significant differences were observed, suggesting proliferation of RGs was not greatly  
246 affected.

247 Overall, these combined results suggest that TBC1D3 expression is no longer able to promote the  
248 generation of bRG-like cells and cycling bRG-like cells in the IZ when Lis1 has previously been  
249 depleted by 50%.

250

### 251 **Lis1 depletion with TBC1D3 expression does not alter Tbr2+ cell numbers**

252

253 We then investigated whether the population of Tbr2+ IPs was also affected in Emx1-Cre Lis1  
254 mutants. Tbr2 and Ki67 co-immunostainings were performed (Figure 4A-D') and cells were  
255 quantified. There were notably no significant differences when considering either the total or the  
256 regional numbers of electroporated Tbr2+ IPs (Figure 4E), Tbr2+ Ki67+ cycling IPs (Figure 4F) or the  
257 ability of Tbr2+ IPs to cycle (Figure 4G), including comparing TBC1D3 WT and TBC1D3 HET

258 conditions. These results suggest that only RG progenitors are affected by *Lis1* depletion, including  
259 when *TBC1D3* is expressed, consistent also with findings reported previously for *Lis1* mutants alone  
260 by Pramparo et al., 2010.

261

### 262 **N-Cadherin expression is perturbed in *Lis1* deficient mice but not upon *TBC1D3* expression**

263

264 To assess how *Lis1* depletion may inhibit the generation of bRG-like cells, we first investigated  
265 whether VZ organization and cell interactions were affected. Indeed, expression of *TBC1D3* in the  
266 mouse was previously shown to decrease the expression of N-Cadherin, and this alteration may  
267 explain how bRG-like cells are generated in this model potentially by delamination (Ju et al., 2016).  
268 No quantifications were previously reported in this study. To test if *Lis1* haploinsufficiency impairs  
269 this mechanism, N-Cadherin staining was performed followed by immunofluorescence intensity  
270 quantification at the ventricular surface. No obvious effect of *TBC1D3* expression on N-Cadherin was  
271 observed in WT animals, contrary to that observed in the original study. However, when *Lis1* was  
272 depleted, and in both control and *TBC1D3* plasmid conditions, a decreased expression of N-Cadherin  
273 was suggested (Figure 5A).

274 Performing quantifications across electroporated areas, in control WT animals, a peak of fluorescence  
275 intensity was detected close to the ventricular surface where N-Cadherin expression is the strongest  
276 (Figure 5B). Two-way Anova for repeated measures showed a significant interaction for fluorescence  
277 intensity between the conditions and distance from the ventricle ( $p < 0.0001$ ). No significant  
278 differences were observed between Control WT and *TBC1D3* WT, showing that *TBC1D3* expression  
279 does not affect N-Cadherin expression. Comparing WT to HET conditions however, we noticed a  
280 tendency for a decrease comparing Control HET to Control WT, and a significant decrease comparing  
281 *TBC1D3* HET to *TBC1D3* WT close to the ventricular surface (Figure 5B). This strongly suggests  
282 that *Lis1* depletion reduces N-Cadherin expression at the ventricular surface.

283 To assess more precisely the effect of *Lis1* depletion and TBC1D3 expression on N-Cadherin  
284 expression at the ventricular surface, we performed measurements outside of cell junctions (“*non-*  
285 *junctions*”) and at cell junctions (“*junctions*”) (Figure 5C, D). Overall, results were similar to those  
286 described above, i.e. Control HET and TBC1D3 HET animals showed lower intensity of fluorescence.  
287 At the *non-junction*, interaction between conditions and distance from the ventricle was significant ( $p$   
288 = 0.0002) and significant differences were observed between TBC1D3 WT and TBC1D3 HET (\*),  
289 between TBC1D3 WT and Control HET (§) and between Control WT and TBC1D3 HET (⊗), in  
290 regions close to the ventricular surface. At *junctions*, the interaction was also significant ( $p=0.0011$ ),  
291 and the overall tendency of HETs having lower intensities as compared to WT equivalent brains was  
292 observed, with TBC1D3 HET showing a significantly lower intensity of fluorescence as compared to  
293 TBC1D3 WT. Overall, these results suggest that *Lis1* depletion alters N-Cadherin expression,  
294 potentially leading to perturbed function of VZ progenitors. Therefore, in order to study more  
295 precisely the cellular cohesion between the progenitors, we performed phalloidin staining *en-face*  
296 imaging in all 4 conditions to identify the F-actin organization at the VZ surface. No obvious defect  
297 was observed in the honeycomb structure surrounding electroporated and non-electroporated cells  
298 (Supplementary Figure 6). Thus, although alterations are observed for N-Cadherin, no obvious  
299 changes of F-actin organization are observed.

300

### 301 **Both *Lis1* depletion and TBC1D3 expression alter ventricular mitoses and spindle orientations**

302

303 We then investigated whether the *Emx1-Cre Lis1* mutation altered other aspects of VZ progenitor cell  
304 function, helping to prevent TBC1D3 expression from inducing the production of bRG-like cells. To  
305 evaluate whether mitosis was affected, PH3 immunostaining was performed and the proportion of  
306 PH3+ mitotic cells quantified (Figure 6A). No significant differences were observed in the overall and  
307 regional proportions of mitotic electroporated cells between the different conditions and genotypes  
308 (Figure 6B). However, when considering the distribution of mitoses in the VZ, we observed that *Lis1*  
309 HET depletion (after electroporation with the control plasmid) promoted significantly more basal

310 abventricular mitoses compared to WT ( $27.6\% \pm 9.1$  for Control WT vs.  $64.6\% \pm 6.6$  for Control  
311 HET,  $p < 0.05$ , Figure 6C), consistent with previous *Lis1* mutation studies (Yingling et al., 2008;  
312 Gambello et al., 2003; Pramparo et al., 2010). TBC1D3 expression in WT animals also promoted an  
313 increased proportion of basal abventricular mitoses ( $27.6\% \pm 9.1$  for Control WT vs.  $62.8\% \pm 5.9$  for  
314 TBC1D3 WT,  $p < 0.05$ ), consistent with the original study (Ju et al., 2016). Interestingly, when  
315 TBC1D3 was expressed in HET animals, the proportion of abventricular mitoses was similar to levels  
316 of HET mice electroporated with the control plasmid, or WT with the TBC1D3 plasmid ( $60.0\% \pm 9.9$   
317 for TBC1D3 HET vs.  $64.6\% \pm 6.6$  for Control HET). Thus, both conditions (Lis1 HET control and  
318 WT TBC1D3) lead to increased proportions of abventricular mitoses individually, and expression of  
319 TBC1D3 combined with Lis1 depletion does not show potentiation of the effect. Since Lis1 HET aRG  
320 mitoses are already perturbed when TBC1D3 is introduced, this may help to explain why bRG-like  
321 cells are not generated in the mutant model.

322 We next decided to assess mitotic spindle orientations in *Lis1* mutants in the presence or absence of  
323 TBC1D3. The angles of division of fluorescent dividing aRGs, in contact with the ventricular surface  
324 and engaged in anaphase, were measured (Figure 6D,E, F). Angle distributions for WT and HET with  
325 control plasmids were akin to what was shown previously (Yingling et al 2008). When Lis1 is  
326 depleted by 50%, a lower angle mean was observed, with an apparently wider variability (Control  
327 WT: mean =  $68.1^\circ$ , standard deviation = 18.36; Control HET: mean =  $54.0^\circ$ , standard deviation =  
328 29.16, Levene test:  $p = 0.068$ ). TBC1D3 expression in WT did not appear to greatly alter mitotic  
329 spindle angles compared to the control plasmid, however when TBC1D3 was expressed in *Lis1* mutant  
330 brains, we observed the same tendency as with the control plasmid, Lis1 depletion induced a lower  
331 angle mean and a wider variance (Figure 6D, TBC1D3 WT: mean =  $61.4^\circ$ , standard deviation = 17.17;  
332 TBC1D3 HET: mean =  $52.4^\circ$ , standard deviation = 31.36, Levene test:  $p = 0.10$ ).

333 The naturally low numbers of electroporated cells performing mitosis at the moment of the sacrifice  
334 and fixation of the embryos prevented further meaningful statistical analyses related to the variability  
335 of the angles. Hence, to provide further insight into the data, angles were clustered in three groups  
336 ( $61^\circ - 90^\circ$  for horizontal divisions,  $31^\circ - 60^\circ$  for oblique divisions and  $1^\circ - 30^\circ$  for vertical divisions,

337 Figure 6E). *Lis1* depletion showed more variable angle values, notably increased values were  
338 observed between 1°-30° (0 % in WTs versus 30 % in HETs), apparently at the expense of 31-60°  
339 angles. Expression of TBC1D3 in WT increased oblique divisions (31-60°, 50 % with TBC1D3 versus  
340 37.5 % with the Control plasmid). TBC1D3 expression in *Lis1* HET brains appeared to further  
341 randomize angles (with values observed of 30 %, 30 % and 40% for 1°-30°, 31°-60° and 61°-90°  
342 respectively, Figure 6F).

343 Thus, early alteration of mitotic spindle angles in *Lis1* HET animals could prevent proper segregation  
344 of cell fate determinants at the time of TBC1D3-induced divisions, which might help explain how *Lis1*  
345 prevents bRG-like cell enrichment in the presence of TBC1D3. Higher magnification analysis of  
346 tdTomato+ cells in the VZ in WT and HET conditions, revealed no major differences in the number of  
347 electroporated cells at the ventricle surface (Supplementary Figure 7), since numerous tdTomato+  
348 cells are in contact with the ventricle in both genotypes, validating the electroporation technique in  
349 *Lis1* HET condition. Nevertheless, some aRGs presented altered morphologies since their somata  
350 appeared more oblique in HETs compared to more vertical in WT, which may explain the differences  
351 observed.

352

## 353 Discussion

354

355 Basal RGs were identified relatively recently and shown to be important for the expansion of the  
356 neocortex in gyrencephalic species (Betizeau et al., 2013; Florio et al., 2015; Hansen et al., 2010; Fietz  
357 et al., 2010; Reillo et al., 2011). However, few studies to-date associate defects in these cells with  
358 cortical malformations, most probably since they are few in the rodent, often used to model these  
359 neurodevelopmental disorders. In order to overcome these limitations, we used genetic tools to  
360 amplify bRG-like cells in the mouse, assessing their production in *Lis1* mouse mutants. Using a newly  
361 developed *Lis1* allele, we show that forebrain-specific conditional KO leads to a severe cortical defect

362 and death in early postnatal stages. Taking advantage of viable heterozygote mice (mimicking the  
363 gene dosage in human patients), we tested the production of bRG-like cells in *Lis1* mutant conditions.  
364 We show that they do not form correctly when *TBC1D3* is expressed in *Lis1* HET mutants. We  
365 demonstrate that *Lis1* HETs show severely perturbed spindle orientations and reduced N-Cadherin  
366 expression from early cortical development which appears to preclude the production of bRG-like  
367 cells. We did not observe N-Cadherin impairments in *TBC1D3* WT animals, differing from a previous  
368 study (Ju et al., 2016). This difference could be due to genetic background, since Ju and colleagues  
369 used C57Bl6 mice, while in our study, *LIS1<sup>fl/+</sup> Emx1-Cre<sup>+/-Cre</sup>* animals had a hybrid FVB/C57Bl6  
370 background.

371 Different Cre-expressing lines have been used previously to deplete *Lis1* (Yingling et al., 2008). Use  
372 of Pax2-Cre with Cre expression starting E8 (Rowitch et al., 1999), expected to impact neuroepithelial  
373 cells, leads to a severe impairment of neuroepithelium function in KO animals, with midbrain and  
374 hindbrain degeneration and highly increased apoptosis in forebrain cells. Similar to *Emx1-Cre* KOs  
375 studied here, pups did not survive after birth. Using GFAP-Cre mice with Cre expression starting at  
376 E12.5 and expected to impact aRGs (Brenner and Messing, 1996) there is a slight decrease of the  
377 cortical thickness in KOs, affecting both deep and superficial neurons, and an almost absent  
378 hippocampus. With the *Emx1-Cre* mouse line, we depleted *Lis1* at an intermediary timepoint (E9.5),  
379 at the beginning of the transition from neuroepithelial cells to aRGs in the forebrain (Gorski et al.,  
380 2002). We observed an almost complete degeneration of the cortical wall in KOs, akin to the Pax2-Cre  
381 phenotype and much stronger than that of GFAP-Cre. This suggests that *Lis1* is critical for the proper  
382 transition from neuroepithelial cells to aRGs, the start of neurogenesis and the correct acquisition of  
383 cell fate.

384 *LIS1* heterozygote mutations in human lead to a spectrum of disorders with varying grades of severity,  
385 ranging from pachygyria with a posterior > anterior gradient to complete agyria, subcortical band  
386 heterotopia and/or microcephaly (Lo Nigro et al., 1997; Leventer et al., 2001; Wynshaw-Boris, 2007;  
387 Romero et al., 2018). Thus, haploinsufficient (or heterozygous) mutations have severe consequences  
388 in human (Di Donato et al., 2017), while depletion by 50% in mice has shown few defects of cortical



389 development (Hirotsune et al., 1998; Gambello et al., 2003; Yingling et al., 2008). In *Lis1* HET  
390 animals in our study, no significant changes were observed in the production, proportions in each zone  
391 or cycling capabilities of RGs or IPs. Neuron production and cortical layering also appeared grossly  
392 unaffected, consistent with previous studies (Gambello et al., 2003; Pramparo et al., 2010). Thus *Lis1*  
393 HET mutation in the mouse from E9.5 only leads to comparatively mild defects, suggesting either the  
394 activation of compensatory factors (Pawlisz et al., 2008; Pramparo et al., 2010), or that in human,  
395 cortical development involves mechanisms not present in the mouse. Indeed, mice are naturally  
396 lissencephalic, while the human cortex is gyrencephalic and much more complex (Borrell, 2019).

397 *TBC1D3* is a hominoid specific gene, present in one copy in the chimpanzee and 8 in human (Hodziec  
398 et al., 2006). By *TBC1D3* overexpression in the mouse (Ju et al., 2016), it is possible to “humanize”  
399 the mouse cortex, enriching it in primate-like cells and therefore potentially sensitizing it to mutations  
400 that have deleterious effects in humans. However, aside from molecular, morphological and functional  
401 characteristics highlighted in the Ju et al., 2016 and our studies, we cannot comment on whether *bona*  
402 *fide* bRGs are produced by the alteration of this single gene, hence we take the precaution of  
403 describing them as bRG-like cells. Single-cell RNA sequencing in this and other models (Penisson et  
404 al., 2019) would shed further light on the bRG identities of these cells. Interestingly, when *TBC1D3* is  
405 overexpressed, HET and WT mice display differences, notably in numbers of bRG-like cells. This  
406 suggests that either production of bRG-like cells from aRGs or their self-amplification, or both are  
407 perturbed. Considering the effects of the *Lis1* mutation on aRG mitotic spindle and N-Cadherin  
408 expression in the VZ, we believe that production is already likely to be perturbed. We also quantified  
409 the proportion of cycling cells among the Pax6+ population in the IZ to assess amplification (Figure  
410 3I), and while we did not observe a significant difference between *TBC1D3* WT and *TBC1D3* HET  
411 conditions, there was nevertheless a tendency suggesting that among the bRG-like cells produced in  
412 each condition, the ones present in *TBC1D3* HET brains may cycle less. Interestingly, it has already  
413 been shown that bRGs have perturbed mitosis in human MDS organoids (Bershteyn et al., 2017),  
414 exhibiting a contiguous deletion of 17p13 including *LIS1*. Our experiments differ since bRG-like cell  
415 production in the *Lis1* HET VZ was tested, thus more specifically involving this single gene mutation

416 and comparing numbers in different zones. It is clearly important to continue testing the role of  
417 *Lis1/LIS1* affecting the production and amplification of this cell type.

418 We focused on bRG-like cell production at mid-cortico genesis in *Lis1* HET mouse mutants. bRG  
419 producing mechanisms have been associated with either alterations of mitosis spindle orientation  
420 leading to more oblique and vertical divisions (Shitamukai et al., 2011; Wong et al., 2015; Wang et al.,  
421 2016; Liu et al., 2017; Kalebic et al., 2018), and/or to detachment from the apical surface via  
422 decreased cell adhesion (Taverna et al., 2014; Ju et al., 2016; Martínez-Martínez et al., 2016;  
423 Narayanan et al., 2018; Tavano et al., 2018). Many of the genes that were described to increase bRG-  
424 like cell generation induce more oblique divisions (Penisson et al., 2019), and mitotic spindle  
425 orientation is a well-described mechanism that may contribute to the fine tuning of aRG daughter cell  
426 fate (LaMonica et al., 2013; Taverna et al., 2014). *Lis1* could contribute to this phenomenon by  
427 regulating dynein-dynactin complex activity (Coquelle et al., 2002; Wang et al., 2013; Htet et al.,  
428 2020), as well as actomyosin-mediated cell membrane contractility, influencing cleavage plane  
429 positioning (Moon et al., 2020). However, the mechanisms by which *TBC1D3* promotes the expansion  
430 of the bRG-like cell pool in the mouse remain poorly understood. *TBC1D3* expression was shown  
431 previously to reduce the expression of N-Cadherin at the ventricular surface, with concomitant  
432 decreased expression of *Trnp1* and activation of the MAPK pathway (Stahl et al., 2013; Ju et al.,  
433 2016). However, the exact mechanisms initiated by these modifications remain unclear (Penisson et  
434 al., 2019) and notably we did not observe reduced N-Cadherin in our experimental conditions. It is  
435 also unclear how the N-Cadherin defects already present in *Lis1* mutant cells influence these processes  
436 to prevent the generation of bRG-like cells, since the junctions seem to be preserved in all conditions.  
437 In organoids derived from MDS patient cells, N-Cadherin expression was also altered in the VZ, as  
438 was spindle orientation, and this phenotype was rescued with *LIS1* re-expression (Iefremova et al.,  
439 2017). This suggests a further role for *LIS1/Lis1*, confirmed by our results, in the orientation of the  
440 mitotic spindle, potentially related to changed adhesion (Bergstrahl et al., 2017), which may be critical  
441 for bRG production. An alternative explanation of our data for the reduction in the production of bRGs  
442 after *TBC1D3* expression may have been purely methodological. Indeed, if a higher proportion of *Lis1*

443 mutant aRGs are detached, they could potentially be missed by *TBC1D3* electroporation (since IUE  
444 targets cells at the ventricular surface) and therefore generate indirectly less bRGs. But our data do not  
445 show obvious changes of aRGs (including numbers electroporated) in the HET condition, which is in  
446 harmony with previous studies (Hirotsune et al., 1998; Gambello et al., 2003; Pawlisz et al., 2008;  
447 Pramparo et al., 2010; Pawlisz et al., 2011). Although we cannot totally rule out the possibility that  
448 some cells have detached, there is no evidence to suggest that this is a major cause of diminished bRG  
449 production in HET animals after *TBC1D3* expression.

450 Both *Lis1* depletion and *TBC1D3* expression led to an increased proportion of abventricular mitoses.  
451 This could have been a readout for progenitor detachment, in fitting with the increased numbers of  
452 bRG-like cells when *TBC1D3* is expressed. However, this phenomenon is not sufficient to explain the  
453 cellular identity of abventricularly dividing cells in *Lis1* mutants. During interkinetic nuclear  
454 migration (Kulikova et al., 2011; Tavano et al., 2018), mitoses take place at the ventricular surface.  
455 Dynein is required for apical migration towards the ventricle (Tsai et al., 2010) and this process may  
456 also be perturbed in *Emx1-Cre Lis1* mutants, increasing the number of ectopically dividing ‘aRGs’. If  
457 apical migration is slower, or severely inhibited, this would increase the number of mitoses away from  
458 the ventricular surface. Such an ectopic position of the nucleus might be expected to impair *TBC1D3*-  
459 inducing mechanisms to generate bRG-like cells, since in our model, *TBC1D3* expression was induced  
460 in aRGs (E14.5), after deletion of *Lis1* (E9.5). Thus, we do not exclude that such ectopic Pax6+  
461 mitoses contribute to impairing bRG-like production, however, as mentioned above, further mitotic  
462 spindle defects were also observed at the ventricular surface in *Lis1* mutants.

463 The effect of *Lis1*’s depletion on mitotic spindle orientation has been well characterized in drosophila,  
464 mice and organoids. When *Lis1* expression is decreased in early apical progenitors (neuroepithelial or  
465 aRGs), performing mainly horizontal divisions (with vertical cleavage planes), they start to engage in  
466 divisions with random angles, including oblique and horizontal angles (Yingling et al., 2008;  
467 Pramparo et al., 2010; Iefremova et al., 2017; Siller et al., 2005, 2008). Furthermore, *LIS1* re-  
468 expression in MDS organoids rescued the mitotic spindle angle phenotype (Iefremova et al., 2017),  
469 showing the importance of this gene for this phenotype. In our study, when comparing Control WT to

470 Control HET, and TBC1D3 WT to TBC1D3 HET, we observed an angle dispersion increase,  
471 associated with the *Lis1* mutation, as well as a small increase in the proportion of oblique divisions in  
472 presence of TBC1D3, but we did not observe more bRG-like cells in the TBC1D3 HETs associated  
473 with this division angle phenotype. It is possible that under *Lis1* mutant conditions, the mitotic spindle  
474 machinery is perturbed, perhaps involving N-Cadherin and dynein function, and TBC1D3 may not be  
475 able to induce a proper segregation of cell fate determinants and / or the maintenance of the basal  
476 process, required for the epithelial fate (Moon et al., 2020). We hypothesize that there is a dichotomy  
477 between a purposeful alteration of mitotic angle, involving TBC1D3's signaling pathway(s), and a  
478 pathological alteration induced by the loss of a major component of the spindle machinery, in this case  
479 *Lis1*. Regulation of mitotic spindle orientation and mitosis progression is managed in part by a *Lis1*-  
480 *Ndel1*-dynein complex (Moon et al., 2014). Similar to the stabilization of microtubules, re-expression  
481 of *Lis1* or overexpression of *Ndel1* or dynein led to rescue of spindle misorientation in *Lis1* mutant  
482 MEFs (Moon et al., 2014). We hence predict that an early rescue of spindle orientation in *Lis1* mutant  
483 aRGs, or a different timing of *Lis1* mutation, might enable TBC1D3 to induce bRG-like cell  
484 production.

485 Our work combined with the previous MDS organoid study (Bershteyn et al., 2017) begins to decipher  
486 bRG mechanisms in *Lis1/MDS* mutant conditions. In our mouse mutant work, only TBC1D3 is  
487 experimentally manipulated, not involving multiple entries into the bRG pathway which occurs  
488 physiologically. Thus, human cells in developing organoids express a larger battery of genes and  
489 signaling pathways involved in the generation of bRGs (Penisson et al., 2019). However, as the state  
490 of bRGs in human pathologies remains understudied, using a single gene such as TBC1D3 in mouse  
491 mutants can be useful for assessing specific pathways, helping us to further understand bRG  
492 mechanisms. bRGs have been suggested to be critical for the correct development of the cortex in  
493 gyrencephalic species, due to their number and proliferative properties. However, whether their  
494 number, distribution or function are perturbed in pathologies in which cortical folding is altered, i.e. in  
495 human lissencephaly, instead of in organoids or mouse models, still remains unknown. Investigating

496 human-like bRG cells induced in mouse models, produced with tools that can even lead to the  
497 generation of mouse cortical folds, can open new windows to study and revisit MCDs.

498

## 499 Materials and Methods

### 500 Animals

501 Research was carried out conforming to national and international directives (directive CE 2010/63 /  
502 EU, French national APAFIS n° 8121) with protocols followed and approved by the local ethical  
503 committee (Charles Darwin, Paris, France). Mice were housed with a light/dark cycle of 12 h (lights  
504 on at 07:00).

505 Swiss wild-type (WT) mice (Janvier Labs, France) were used for *in utero* electroporation to confirm  
506 the TBC1D3 effect on bRG-like cell production (Ju et al., 2016). For the study of Lis1 depletion, Lis1  
507 floxed allele mice (Hirotsune et al., 1998) maintained on the FVB background from which the neo  
508 selection cassette had been removed (obtained from Osaka University) were crossed with C57Bl6J  
509 Emx1-Cre knockin animals (Gorski et al., 2002). The Rosa26-EGFP<sup>RCE/RCE</sup> mouse line was used as  
510 reporter (Sousa et al., 2009). All mice were housed in the IFM institute animal facility or at the CDTA,  
511 Orléans, France.

512 Genotyping of all transgenic mouse lines was performed via PCR using these oligonucleotides:

Lis1	Lis1_LoxP5: CCT CTA CCA CTA AAG CTT GTT
	Lis1_LoxP3: TGA ATG CAT CAG AAC CAT GC
Emx1-Cre	Cre_forward: GGA CAT GTT CAG GGA TCG CCA GGC G
	Cre_reverse: GCA TAA CCA GTG AAA CAG CAT TGC TG
Rosa26-EGFP	Rosa_1: CCC AAA GTC GCT CTG AGT TGT TAT C
	Rosa_2: GAA GGA GCG GGA GAA ATC GAT ATG
	Cag3: CCA GGC GGG CCA TTT ACC GTA AG

513

## 514 Plasmid preparation

515

516 Plasmids were amplified from NEB 5 $\alpha$  bacterial cultures transformed with pCS2-cMyc-TBC1D3  
517 (gratefully received from Zhen-Ge Luo's team), pCS2-cMYC-Control (generated from the TBC1D3  
518 construct) or pCAG-IRES-TdTomato plasmids (kindly provided by C. Lebrand, Lausanne), all of  
519 which carried the ampicillin resistance gene. These were cultured overnight (O/N) on petri dishes  
520 containing culture medium and ampicillin (50 mg/L). Clones were then amplified and cultured in 200  
521 mL LB medium + ampicillin (50 mg/L) O/N. Plasmid DNAs were then extracted using the  
522 NucleoBond™ Xtra midi EF kit (Fisher Scientific), following the recommended protocol. After  
523 extraction, plasmid preparations were resuspended in endonuclease-free H<sub>2</sub>O at approximately 5  
524  $\mu\text{g}/\mu\text{L}$ , concentrations verified with spectrophotometry (NanoDrop 1000 spectrophotometer, Thermo  
525 Scientific) and stored at -20°C.

526

## 527 Electroporation in utero

528

529 E14.5 pregnant females were anaesthetized with 4 % isoflurane (Baxter) and a Minerve Dräger Vapor  
530 2000 apparatus, and maintained on a heating pad at 37°C at 2-3% isoflurane depending on animal  
531 weight and respiratory rhythm. The abdomen of the animals was sectioned and uterine horns were  
532 extracted and kept hydrated with NaCl 0.9% (Braun) + penicillin streptomycin (P/S, 10 mg/mL). A  
533 plasmid solution (DNA concentration of 1  $\mu\text{g}/\mu\text{l}$  + Fast-Green 1% (F-7258, Sigma)) was then injected  
534 in the lateral ventricles of the embryos with glass micropipettes. Micropipettes were generated from  
535 glass capillaries (GC150TF-10, Harvard Apparatus) that were pulled using a Narishige PC-100 pipette  
536 puller. Electrodes (CUY650P3, NepaGene) were placed on the sides of the head of embryos in such a  
537 way as to propagate entry of the plasmid in the pallium. Electroporation was performed with 5 pulses  
538 of 35 V, each with a duration of 50 ms, and with 950 ms intervals using a CUY21 (NepaGene)  
539 electroporator. The uterus was then replaced carefully inside the mother's abdomen, the inside of the

540 abdomen was washed with NaCl 0.9% + P/S solution and the wound was closed with stitches using  
541 Vycril thread (VICRYL JV390, ETHICON) for the muscle wall, and, Ethilon thread (ETHILON  
542 F3206, ETHICON) for the skin. Mice were injected subcutaneously with Flunixin (4 mg/kg) and put  
543 back in their cage on a heating pad at 37 °C to recuperate with monitoring.

544

## 545 [Brain slicing, histology, immunofluorescence and confocal acquisition](#)

546

547 Females that underwent *in utero* electroporation were sacrificed 48 hours later, and brains of embryos  
548 were collected and fixed in 4 % paraformaldehyde overnight at 4 °C. Brains were then rinsed and  
549 conserved in 1X PBS (diluted from PBS 10X, ET330 Euromedex) + 0.1 % azide (S200-2, Sigma-  
550 Aldrich). Prior to Vibratome sectioning, brains were embedded in an 8 % sucrose (200-301-B,  
551 Euromedex), 6 % agarose (LE-8200-B, Euromedex) PBS solution. Serial 50 µm thick coronal sections  
552 were performed with a VT1000S vibratome (Leica). For immunofluorescence labelling, 2 to 3 slices  
553 per brain were used for every experiment. Saturation and permeabilization was performed for 1 hour  
554 with a 10 % normal goat serum (NGS) (16210072, Gibco) and 0.1 % Triton X-100 (T9284, Sigma)  
555 solution in 1X PBS, then slices were incubated with primary antibodies O/N (or for 72 hours for Ki67)  
556 diluted in permeabilization and saturation buffer at 4 °C under agitation. Primary antibodies include c-  
557 Myc-Tag (71D10, #2278, Cell Signalling, 1:400), Pax6 (Biolegend, BLE901301, 1:300), PH3  
558 (Millipore, 06-570, 1:400), Tbr2 (AB23345, Abcam, 1:300), Tbr1 (grateful gift from Robert Hevner,  
559 1:1000), aCas3 (559565, BD Pharmingen, 1:250), Ki67 (BD Biosciences, 556003, 1:300), N-Cadherin  
560 (BD Biosciences, 610920, 1:500). Ki67 antibody required antigen retrieval: prior to permeabilization  
561 and saturation, slices were incubated in 10 mM sodium citrate, 0.05 % Tween pH 6.0 at 95 °C for 20  
562 minutes, then left to cool down at room temperature before rinsing 3 times with 1X PBS. After  
563 incubation with primary antibodies, slices were rinsed 3 times with permeabilization and saturation  
564 buffer. Secondary antibodies were then incubated at 1:800 dilution for 2 hours at room temperature  
565 under agitation, the list include donkey-anti-rabbit Alexa 488 (ThermoFisher, A21206), donkey-anti-

566 mouse Alexa 488 (ThermoFisher, A21201), donkey-anti-rabbit Alexa 647 (ThermoFisher A31573).  
567 Slices were then rinsed with Hoechst (33258, Sigma) 1:10000 for 10 minutes diluted in 1X PBS, and  
568 then rinsed twice with 1X PBS. Slices were mounted on Superfrost Plus microscopic slides (Thermo  
569 Scientific) with Fluoromount-G (Invitrogen). Confocal acquisitions were performed with an SP-5  
570 Leica microscope (x40), stacks of 30-40  $\mu\text{m}$  were performed.

571 *En face* VZ staining was performed as described previously in Bizzotto et al., 2017. Briefly, E16.5  
572 mouse embryonic brains were fixed in 4 % paraformaldehyde (Sigma-Aldrich, France) O/N at 4°C.  
573 Cortical explants were dissected and incubated with Alexa Fluor 488 Phalloidin (1:100, Life  
574 Technologies) in PBST 1% O/N at RT. Extensive washing was performed in PBST 1% before  
575 mounting the explants with Fluoromount G (Life Technologies) with the ventricular surface up to  
576 obtain an *en face* view of the ventricular side of the cortex. Confocal images were acquired with a  
577 0.3  $\mu\text{m}$  z-stack depth for a total depth of 5  $\mu\text{m}$  (TCS Leica SP5-II).

578 For studies in mouse pups (P0), animals were rapidly decapitated, and brains were removed and  
579 postfixed in 4% paraformaldehyde overnight at 4°C and then stored in PBS. Then, dissected brains  
580 were embedded in 6% agarose and 8% sucrose. 50- $\mu\text{m}$  coronal sections were prepared using a  
581 vibratome (VT1000S; Leica), Nissl staining was performed on sections mounted on Superfrost slides  
582 (Thermo Fisher). The sections were analyzed with a brightfield microscope (Provis; Olympus) using a  
583 charge-coupled device (CCD) camera (CoolSNAP CF; Photometrics) and 4 $\times$  (NA = 0.13) objective.

584

## 585 [Analysis](#)

586

587 Quantification for tdTomato, Pax6, Tbr1, Tbr2, Ki67, aCas3 and PH3, as well as for mitotic spindle  
588 angles was performed using Icy Bioimage software. tdTomato quantification was performed by  
589 counting each individual cell, and c-Myc+, Pax6+, Tbr1+, Ki67+ and PH3+ nuclei were counted  
590 amongst tdTomato+ cells. Quantification for aCas3 involved counting clusters of aCas3 staining,  
591 representing cell debris. Regions of interest (VZ, SVZ, IZ, CP) were defined in actual, adjacent or



592 similar level sections using Hoechst, Pax6, Sox2 and/or Tbr2 staining. The VZ was defined using Pax6  
593 staining, the IZ was characterized as a region of lower cell density using Hoechst, and the SVZ was  
594 defined either by Tbr2 staining or as the region lying in between predefined VZ and IZ. Cells  
595 positively stained for tdTomato and nuclear markers, or aCas3 clusters, were counted with the  
596 “Manual Counting” plug-in according to their localization. Results are shown as a percentage of  
597 tdTomato cells, to account for variabilities in efficiency of *in utero* electroporation. Quantification for  
598 N-Cadherin fluorescence intensity was performed using Fiji software. Ten 10  $\mu\text{m}$  lines were drawn  
599 perpendicular to and across the ventricular surface such that the bottom of each line (10<sup>th</sup>  $\mu\text{m}$ ) was at  
600 the transition between the ventricle and the ventricular surface. Five lines were drawn at the junction  
601 between 2 cells, and 5 not at the junction (i.e. in the middle of cells). Fluorescence intensity curves  
602 were calculated using the multi plot feature in ROI manager for each line, and pixel intensity was  
603 measured every  $\mu\text{m}$  all along the 10  $\mu\text{m}$  lines. The means curves of the 5 lines for the junctions, 5 lines  
604 for the non-junctions and 10 in total per image were then calculated for each brain, and then compared  
605 between conditions for statistical analysis. Cortical thickness was measured using Fiji software. 3 lines  
606 per hemisphere were drawn, and the mean was calculated. Statistical analyses were performed using R  
607 and the Rcmdr graphical interface, and Prism software (GraphPad). Normality of residuals and  
608 homoscedasticity were checked with Shapiro and Levene tests respectively prior to performing any  
609 parametrical test (*t*-tests, one-way and two-way ANOVAs).

610

## 611 Acknowledgements

612 We thank I. Moutkine, Dr. D. Romero, Dr. M. Stouffer, Dr. A. Uzquiano, A. Diakite and A. Houllier  
613 for experimental help. We are grateful to the following people for kindly gifting us materials: Dr. Z-G  
614 Luo for the pCS2-cMyc-TBC1D3 plasmid; Dr C. Lebrand for the CAG-Tomato plasmid, Dr. M.  
615 Groszer for provision of the Emx1-Cre line and Dr K. Jones for agreement to use this line. We thank  
616 the animal experimentation facility and cellular and tissue imaging platforms at the Institut du Fer à  
617 Moulin (IFM), supported also by the Région Ile de France and the FRC Rotary. We thank G. Grannec

618 (IFM), L. Stoica (IFM) and the TAAM (CDTA Orleans) for aid with the maintenance and rederivation  
619 of mouse lines. Our salaries and labs were supported by Inserm; Centre National de la Recherche  
620 Scientifique (CNRS); Sorbonne University; the ERA-Net NEURON JTC 2015 Neurodevelopmental  
621 Disorders program affiliated with the French Agence National de la Recherche (ANR, NEURON8-  
622 Full-815- 006 STEM-MCD, including PhD student salary for MP), the French Fondation Bettencourt  
623 Schueller; the European Union (EU-HEALTH-2013, DESIRE, number 60253); and the European  
624 Cooperation in Science and Technology (COST Action CA16118). This project was further supported  
625 by the French ANR under the frame of E-Rare-3, the ERA-Net for Research on Rare Diseases  
626 (ERARE18-049). We particularly thank STEM-MCD participants for their contribution to this work.  
627 MP, RB and F.F. were associated with the BioPsy Labex project, the Ecole des Neurosciences de Paris  
628 Ile-de-France (ENP) network, and the Sorbonne University Complexité du Vivant doctoral school.  
629

## 630 **References**

631

632 Agirman, G., Broix, L., and Nguyen, L. (2017). Cerebral cortex development: an outside-in  
633 perspective. *FEBS Lett.* **591**, 3978–3992. doi:10.1002/1873-3468.12924.

634 Barkovich, A. J., Guerrini, R., Kuzniecky, R. I., Jackson, G. D., and Dobyns, W. B. (2012). A  
635 developmental and genetic classification for malformations of cortical development:  
636 Update 2012. *Brain* **135**, 1348–1369. doi:10.1093/brain/aws019.

637 Bergstralh, D. T., Dawney, N. S. and St Johnston, D. (2017). Spindle orientation: A question of  
638 complex positioning. *Development* **144**, 1137–1145.

639 Bershteyn, M., Nowakowski, T.J., Pollen, A.A., Di Lullo, E., Nene, A., Wynshaw-Boris, A. and  
640 Kriegstein, A.R. (2017). Human iPSC-Derived Cerebral Organoids Model Cellular Features  
641 of Lissencephaly and Reveal Prolonged Mitosis of Outer Radial Glia. *Cell Stem Cell*, **20**,  
642 435-449 e434. doi:10.1016/j.stem.2016.12.007.

643 Betizeau, M., Cortay, V., Patti, D., Pfister, S., Gautier, E., Bellemin-Menard, A., Afanassieff, M.,  
644 Huissoud, C., Douglas, R.J., Kennedy, H. *et al.* (2013) Precursor diversity and complexity  
645 of lineage relationships in the outer subventricular zone of the primate. *Neuron*, **80**, 442-  
646 457. doi:10.1016/j.neuron.2013.09.032.

647 Bizzotto, S., Uzquiano, A., Dingli, F., Ershov, D., Houllier, A., Arras, G., Richards, M., Loew,  
648 D., Minc, N., Croquelois, A. *et al.* (2017) Eml1 loss impairs apical progenitor spindle  
649 length and soma shape in the developing cerebral cortex. *Sci. Rep.*, **7**, 17308.

650 Borrell, V. (2019). Recent advances in understanding neocortical development. *F1000Research*.  
651 **23**. doi:10.12688/f1000research.20332.1.

652 Brenner, M., and Messing, A. (1996). GFAP Transgenic Mice. *Methods* **10**, 351–364.

653 Capuano, P., Cialdella, M., and D’addario, V. (2017). Malformations of cortical development.  
654 *Donald School J. Ultrasound Obstet. Gynecol.* **11**, 308–313. doi:10.5005/jp-journals-  
655 10009-1538.

656 Cianfrocco, M. A., Desantis, M. E., Leschziner, A. E. and Reck-Peterson, S. L. (2015).  
657 Mechanism and Regulation of Cytoplasmic Dynein. *Annu. Rev. Cell Dev. Biol* **31**, 83–108.

658 Coquelle, F.M., Caspi, M., Cordelieres, F.P., Dompierre, J.P., Dujardin, D.L., Koifman, C.,  
659 Martin, P., Hoogenraad, C.C., Akhmanova, A., Galjart, N. *et al.* (2002). LIS1, CLIP-170's  
660 key to the dynein/dynactin pathway. *Mol. Cell. Biol.*, **22**, 3089-3102.  
661 doi:10.1128/mcb.22.9.3089-3102.2002.

662 Desikan, R. S., and Barkovich, J. (2016). Malformations of cortical development. *Ann. Neurol.*  
663 **80**, 797–810. doi:10.5005/jp-journals-10009-1538.

664 Di Donato, N., Chiari, S., Mirzaa, G.M., Aldinger, K., Parrini, E., Olds, C., Barkovich, A.J.,  
665 Guerrini, R. and Dobyns, W.B. (2017). Lissencephaly: Expanded imaging and clinical  
666 classification. *Am. J. Med. Genet. A*, **173**, 1473-1488. doi:10.1002/ajmg.a.38245.

667 Dobyns, W. B., Reiner, O., Carrozzo, R., and Ledbetter, D. H. (1993). Lissencephaly: A Human  
668 Brain Malformation Associated With Deletion of the LIS1 Gene Located at Chromosome  
669 17p13. *JAMA* **270**, 2838–2842. doi:10.1001/jama.270.23.2838.

670 Fietz, S.A., Kelava, I., Vogt, J., Wilsch-Brauninger, M., Stenzel, D., Fish, J.L., Corbeil, D.,  
671 Riehn, A., Distler, W., Nitsch, R. *et al.* (2010). OSVZ progenitors of human and ferret  
672 neocortex are epithelial-like and expand by integrin signaling. *Nat. Neurosci.*, **13**, 690-699.

673 Florio, M., Albert, M., Taverna, E., Namba, T., Brandl, H., Lewitus, E., Haffner, C., Sykes, A.,  
674 Wong, F.K., Peters, J. *et al.* (2015). Human-specific gene ARHGAP11B promotes basal  
675 progenitor amplification and neocortex expansion. *Science*, **347**, 1465-1470.  
676 doi:10.1126/science.aaa1975.

677 Gambello, M. J., Darling, D. L., Yingling, J., Tanaka, T., Gleeson, J. G. and Wynshaw-Boris, A.  
678 (2003). Multiple Dose-Dependent Effects of Lis1 on Cerebral Cortical Development. *J.*  
679 *Neurosci.* **23**, 1719–1729.

680 Gorski, J. A., Talley, T., Qiu, M., Puellas, L., Rubenstein, J. L. R., and Jones, K. R. (2002).  
681 Cortical excitatory neurons and glia, but not GABAergic neurons, are produced in the  
682 Emx1-expressing lineage. *J. Neurosci.* **22**, 6309–6314. doi:10.1523/jneurosci.22-15-  
683 06309.2002.

684 Götz, M., and Huttner, W. B. (2005). The cell biology of neurogenesis. *Nat. Rev. Mol. Cell Biol.*  
685 **6**, 777–788. doi:10.1038/nrm1739.

686 Hansen, D. V, Lui, J. H., Parker, P. R. L., and Kriegstein, A. R. (2010). Neurogenic radial glia in  
687 the outer subventricular zone of human neocortex. *Nature* **464**, 554–561.  
688 doi:10.1038/nature08845.

689 Heng, X., Guo, Q., Leung, A. W., and Li, J. Y. H. (2017). Analogous mechanism regulating  
690 formation of neocortical basal radial glia and cerebellar Bergmann glia. *eLife* **6**, 1–30.  
691 doi:10.7554/eLife.23253.

692 Hevner, R. F. (2019). Intermediate progenitors and Tbr2 in cortical development. *J. Anat.* **235**,  
693 616–625. doi:10.1111/joa.12939.

694 Hirotsune, S., Fleck, M.W., Gambello, M.J., Bix, G.J., Chen, A., Clark, G.D., Ledbetter, D.H.,  
695 McBain, C.J. and Wynshaw-Boris, A. (1998). Graded reduction of Pafah1b1 (Lis1) activity  
696 results in neuronal migration defects and early embryonic lethality. *Nat. Genet.* **19**, 333-  
697 339. doi:10.1038/1221.

698 Hodzic, D., Kong, C., Wainszelbaum, M. J., Charron, A. J., Su, X., and Stahl, P. D. (2006).  
699 TBC1D3 , a hominoid oncoprotein , is encoded by a cluster of paralogues located on  
700 chromosome 17q12. *Genomics* **88**, 731–736. doi:10.1016/j.ygeno.2006.05.009.

701 Htet, Z. M., Gillies, J. P., Baker, R. W., Leschziner, A. E., DeSantis, M. E., and Reck-Peterson,  
702 S. L. (2020). LIS1 promotes the formation of activated cytoplasmic dynein-1 complexes.  
703 *Nat. Cell Biol.* **22**, 518–525. doi:10.1038/s41556-020-0506-z.

704 Iefremova, V., Manikakis, G., Krefft, O., Jabali, A., Weynans, K., Wilkens, R., Marsoner, F.,  
705 Brandl, B., Muller, F.J., Koch, P. *et al.* (2017). An Organoid-Based Model of Cortical  
706 Development Identifies Non-Cell-Autonomous Defects in Wnt Signaling Contributing to  
707 Miller-Dieker Syndrome. *Cell Rep.* **19**, 50-59. doi:10.1016/j.celrep.2017.03.047.

708 Ju, X.C., Hou, Q.Q., Sheng, A.L., Wu, K.Y., Zhou, Y., Jin, Y., Wen, T., Yang, Z., Wang, X. and  
709 Luo, Z.G. (2016). The hominoid-specific gene TBC1D3 promotes generation of basal  
710 neural progenitors and induces cortical folding in mice. *Elife*, **5**, 1–25.  
711 doi:10.7554/eLife.18197.

712 Kalebic, N., Gilardi, C., Albert, M., Namba, T., Long, K.R., Kostic, M., Langen, B. and Huttner,  
713 W.B. (2018). Human-specific ARHGAP11B induces hallmarks of neocortical expansion in  
714 developing ferret neocortex. *Elife*, **7**, 395830. doi:10.7554/eLife.41241.

715 Kulikova, S., Abatis, M., Heng, C., and Lelievre, V. (2011). Interkinetic nuclear migration:  
716 Reciprocal activities of dynein and kinesin. *Cell Adh. Migr.* **5**, 277–279.  
717 doi:10.4161/cam.5.4.17432.

718 LaMonica, B. E., Lui, J. H., Hansen, D. V, and Kriegstein, A. R. (2013). Mitotic spindle  
719 orientation predicts outer radial glial cell generation in human neocortex. *Nat. Commun.* **4**.  
720 doi:10.1038/ncomms2647.

721 LaMonica, B. E., Lui, J. H., Wang, X., and Kriegstein, A. R. (2012). OSVZ progenitors in the  
722 human cortex: An updated perspective on neurodevelopmental disease. *Curr. Opin.*  
723 *Neurobiol.* **22**, 747–753. doi:10.1016/j.conb.2012.03.006.

724 Leventer, R. J., Cardoso, C., Ledbetter, D. H., and Dobyns, W. B. (2001). LIS1 missense  
725 mutations cause milder lissencephaly phenotypes including a child with normal IQ.  
726 *Neurology* **57**, 416–422. doi:10.1212/WNL.57.3.416.

727 Liu, J., Liu, W., Yang, L., Wu, Q., Zhang, H., Fang, A., Li, L., Xu, X., Sun, L., Zhang, J. *et al.*  
728 (2017). The Primate-Specific Gene TMEM14B Marks Outer Radial Glia Cells and  
729 Promotes Cortical Expansion and Folding. *Cell Stem Cell* **21**, 635-649 e638.  
730 doi:10.1016/j.stem.2017.08.013.

731 Lo Nigro, C., Chong, S. S., Smith, A. C. M., Dobyns, W. B., Carrozzo, R., and Ledbetter, D. H.  
732 (1997). Point mutations and an intragenic deletion in LIS1, the lissencephaly causative gene  
733 in isolated lissencephaly sequence and Miller-Dieker syndrome. *Hum. Mol. Genet.* **6**, 157–  
734 164. doi:10.1093/hmg/6.2.157.

735 Lui, J. H., Nowakowski, T. J., Pollen, A. A., Javaherian, A., Kriegstein, A. R., and Oldham, M.  
736 C. (2014). Radial glia require PDGFD–PDGFRb signalling in human but not mouse  
737 neocortex. *Nature* **515**, 264-8. doi:10.1038/nature13973.

738 Martínez-Martínez, M. Á., de Juan Romero, C., Fernández, V., Cárdenas, A., Götz, M., and  
739 Borrell, V. (2016). A restricted period for formation of outer subventricular zone defined by  
740 Cdh1 and Trnp1 levels. *Nat. Commun.* **7**. doi:10.1038/ncomms11812.

741 Wynshaw-Boris, A. (2007). Lissencephaly and LIS1: insights into the molecular mechanisms of  
742 neuronal migration and development. *Clin. Genet.* **72**, 296–304. doi:10.1111/j.1399-  
743 0004.2007.00888.x.

744 Moon, H. M., Hippenmeyer, S., Luo, L., and Wynshaw-Boris, A. (2020). LIS1 determines  
745 cleavage plane positioning by regulating actomyosin-mediated cell membrane contractility.  
746 *eLife* **9**, 1–31. doi:10.7554/eLife.51512.

747 Moon, H. M., Youn, Y. H., Pemble, H., Yingling, J., Wittmann, T., and Wynshaw-Boris, A.  
748 (2014). LIS1 controls mitosis and mitotic spindle organization via the LIS1-NDEL1-dynein  
749 complex. *Hum. Mol. Genet.* **15**,449-466. doi:10.1093/hmg/ddt436.

750 Narayanan, R., Pham, L., Kerimoglu, C., Watanabe, T., Castro Hernandez, R., Sokpor, G.,  
751 Ulmke, P.A., Kiszka, K.A., Tonchev, A.B., Rosenbusch, J. *et al.* (2018). Chromatin  
752 Remodeling BAF155 Subunit Regulates the Genesis of Basal Progenitors in Developing  
753 Cortex. *iScience*, **4**, 109-126. doi:10.1016/j.isci.2018.05.014.

754 Pawlisz, A. S. and Feng, Y. (2011). Three-dimensional regulation of radial glial functions by  
755 lis1-nde1 and dystrophin glycoprotein complexes. *PLoS Biol.* **9**, e1001172. doi:  
756 10.1371/journal.pbio.1001172..

757 Pawlisz, A. S., Mutch, C., Wynshaw-Boris, A., Chenn, A., Walsh, C. A. and Feng, Y. (2008).  
758 Lis1-Nde1-dependent neuronal fate control determines cerebral cortical size and  
759 lamination. *Hum. Mol. Genet.* **17**, 2441–2455.

760 Penisson, M., Ladewig, J., Belvindrah, R., and Francis, F. (2019). Genes and Mechanisms  
761 Involved in the Generation and Amplification of Basal Radial Glial Cells. *Front. Cell.*  
762 *Neurosci.* **13**, 1–21. doi:10.3389/fncel.2019.00381.

763 Pilz, G.A., Shitamukai, A., Reillo, I., Pacary, E., Schwausch, J., Stahl, R., Ninkovic, J., Snippert,  
764 H.J., Clevers, H., Godinho, L. *et al.* (2013). Amplification of progenitors in the mammalian  
765 telencephalon includes a new radial glial cell type. *Nat. Commun.* **4**, 2125.  
766 doi:10.1038/ncomms3125.

767 Pramparo, T., Youn, Y. H., Yingling, J., Hirotsune, S., and Wynshaw-Boris, A. (2010). Novel  
768 embryonic neuronal migration and proliferation defects in Dcx mutant mice are exacerbated  
769 by Lis1 reduction. *J. Neurosci.* **30**, 3002–3012. doi:10.1523/JNEUROSCI.4851-09.2010.

770 Reillo, I., De Juan Romero, C., García-Cabezas, M. Á., and Borrell, V. (2011). A Role for  
771 intermediate radial glia in the tangential expansion of the mammalian cerebral cortex.  
772 *Cereb. Cortex* **21**, 1674–1694. doi:10.1093/cercor/bhq238.

773 Reiner, O., and Sapir, T. (2013). LIS1 functions in normal development and disease. *Curr. Opin.*  
774 *Neurobiol.* **23**, 951–956. doi:10.1016/j.conb.2013.08.001.

775 Romero, D. M., Bahi-Buisson, N., and Francis, F. (2018). Genetics and mechanisms leading to  
776 human cortical malformations. *Semin. Cell Dev. Biol.* **76**, 33–75.  
777 doi:10.1016/j.semcdb.2017.09.031.

778 Rowitch, D. H., Kispert, A., and McMahon, A. P. (1999). Pax-2 regulatory sequences that direct  
779 transgene expression in the developing neural plate and external granule cell layer of the  
780 cerebellum. *Brain Res. Dev. Brain Res.* **20**, 99-108. doi:10.1016/S0165-3806(99)00104-2.

781 Shitamukai, A., Konno, D. and Matsuzaki, F. (2011). Oblique Radial Glial Divisions in the  
782 Developing Mouse Neocortex Induce Self-Renewing Progenitors outside the Germinal  
783 Zone That Resemble Primate Outer Subventricular Zone Progenitors. *J. Neurosci.* **31**,  
784 3683–3695.

785 Siller, K. H. and Doe, C. Q. (2008). Lis1/dynactin regulates metaphase spindle orientation in  
786 *Drosophila* neuroblasts. *Dev. Biol.* **319**, 1–9.

787 Siller, K. H., Serr, M., Steward, R., Hays, T. S. and Doe, C. Q. (2005). Live imaging of



788 Drosophila brain neuroblasts reveals a role for Lis1/dynactin in spindle assembly and  
789 mitotic checkpoint control. *Mol. Biol. Cell.* **16**, 5127-40.

790 Sousa, V. H., Miyoshi, G., Hjerling-Leffler, J., Karayannis, T., and Fishell, G. (2009).  
791 Characterization of Nkx6-2-derived neocortical interneuron lineages. *Cereb. Cortex* **19**, 1–10.  
792 doi:10.1093/cercor/bhp038.

793 Stahl, R., Walcher, T., De Juan Romero, C., Pilz, G.A., Cappello, S., Irmeler, M., Sanz-Aquila,  
794 J.M., Beckers, J., Blum, R., Borrell, V. *et al.* (2013). Trnp1 regulates expansion and folding  
795 of the mammalian cerebral cortex by control of radial glial fate. *Cell* **153**, 535-549.  
796 doi:10.1016/j.cell.2013.03.027.

797 Subramanian, L., Calcagnotto, M. E., and Paredes, M. F. (2020). Cortical Malformations :  
798 Lessons in Human Brain Development. *Front. Cell. Neurosci.* **13**, 1–17.  
799 doi:10.3389/fncel.2019.00576.

800 Tavano, S., Taverna, E., Kalebic, N., Haffner, C., Namba, T., Dahl, A., Wilsch-Brauninger, M.,  
801 Paridaen, J. and Huttner, W.B. (2018). Insm1 Induces Neural Progenitor Delamination in  
802 Developing Neocortex via Downregulation of the Adherens Junction Belt-Specific Protein  
803 Plekha7. *Neuron* **97**, 1299-1314 e1298. doi:10.1016/j.neuron.2018.01.052.

804 Taverna, E., Götz, M., and Huttner, W. B. (2014). The Cell Biology of Neurogenesis: Toward an  
805 Understanding of the Development and Evolution of the Neocortex. *Annu. Rev. Cell Dev.*  
806 *Biol.* **30**, 465-502. doi:10.1146/annurev-cellbio-101011-155801.

807 Tsai, J. W., Chen, Y., Kriegstein, A. R., and Vallee, R. B. (2005). LIS1 RNA interference blocks  
808 neural stem cell division, morphogenesis, and motility at multiple stages. *J. Cell Biol.* **170**,  
809 935–945. doi:10.1083/jcb.200505166.

810 Tsai, J. W., Lian, W. N., Kemal, S., Kriegstein, A. R., and Vallee, R. B. (2010). Kinesin 3 and  
811 cytoplasmic dynein mediate interkinetic nuclear migration in neural stem cells. *Nat.*  
812 *Neurosci.* **13**, 1463–1472. doi:10.1038/nn.2665.

813 Wang, L., Hou, S., and Han, Y. G. (2016). Hedgehog signaling promotes basal progenitor  
814 expansion and the growth and folding of the neocortex. *Nat. Neurosci.* **19**, 888–896.  
815 doi:10.1038/nn.4307.

816 Wang, S., Ketcham, S.A., Schon, A., Goodman, B., Wang, Y., Yates, J., 3rd, Freire, E., Schroer,  
817 T.A. and Zheng, Y. (2013). Nudel/NudE and Lis1 promote dynein and dynactin interaction  
818 in the context of spindle morphogenesis. *Mol. Biol. Cell.* **24**, 3522-3533.  
819 doi:10.1091/mbc.E13-05-0283.

820 Wang, X., Tsai, J.-W., LaMonica, B., and Kriegstein, A. R. (2011). A new subtype of progenitor  
821 cell in the mouse embryonic neocortex. *Nat. Neurosci.* **14**, 555–561. doi:10.1038/nn.2807.

822 Wong, F.K., Fei, J.F., Mora-Bermudez, F., Taverna, E., Haffner, C., Fu, J., Anastassiadis, K.,  
823 Stewart, A.F. and Huttner, W.B. (2015). Sustained Pax6 Expression Generates Primate-like  
824 Basal Radial Glia in Developing Mouse Neocortex. *PLoS Biol.* **13**, e1002217.  
825 doi:10.1371/journal.pbio.1002217.

826 Yingling, J., Toyo-oka, K., and Wynshaw-Boris, A. (2003). Miller-Dieker Syndrome: Analysis  
827 of a Human Contiguous Gene Syndrome in the Mouse. *Am. J. Hum. Genet.* **73**, 475–488.  
828 doi:10.1086/378096.

829 Yingling, J., Youn, Y.H., Darling, D., Toyo-Oka, K., Pramparo, T., Hirotsune, S. and Wynshaw-  
830 Boris, A. (2008). Neuroepithelial stem cell proliferation requires LIS1 for precise spindle  
831 orientation and symmetric division. *Cell*, **132**, 474-486. doi:10.1016/j.cell.2008.01.026.  
832  
833

834

835 **FIGURES:**

836

837 **Figure 1: TBC1D3 expression leads to the amplification of Pax6+ cells and the generation of**  
838 **bRG-like cells. A)** Schematic view of the protocol and constructs used for experiments in this figure:  
839 WT embryos (Swiss genetic background) were electroporated at E14.5 and sacrificed at E16.5. Both  
840 electroporated plasmids are represented: pCAG-IRES-tdTomato and pCS2-cMyc-TBC1D3. **B,B',B''**)  
841 Pax6 immunohistochemistry (blue) of E16.5 electroporated mouse brains. Control (tdTomato, B) and  
842 TBC1D3 (tdTomato + TBC1D3, B') electroporated plasmids (arrowheads point to Pax6+ bRG-like  
843 cells in different regions of the cortical wall). Enlargement shows a Pax6+ bRG-like cell with typical  
844 morphology and showing a long basal process (arrows, B''). **C)** Proportion of Pax6+ tdTomato+ /  
845 tdTomato+ cells in each cortical region and in the whole cortex ('Total') per ROI in control (grey  
846 bars) or TBC1D3 (black bars) electroporated brains (3 x 50 µm slices per brain, 3 animals per  
847 condition, 2-way ANOVA with Bonferoni *post hoc*, \* : p<0,05, \*\* : p<0,01). **D,D')** PH3  
848 immunohistochemistry (blue) of E16.5 electroporated mouse brains. Control (tdTomato, D) and  
849 TBC1D3 (tdTomato + TBC1D3, D'). **E)** Proportion of PH3+ tdTomato+ / tdTomato+ in each cortical  
850 region and in the whole cortex ('Total') per ROI in Control or TBC1D3 electroporated brains (3 x 50  
851 µm slices per brain, 3 animals per condition, 2-way ANOVA with Bonferoni *post hoc*, \*\* : p<0,01,  
852 \*\*\* : p<0.001). Note the overall increase of mitoses in TBC1D3 electroporated brains. **F)** Distribution  
853 of ventricular mitoses versus abventricular mitoses (3 x 50 µm slices per brain, 3 animals per  
854 condition, *t*-test, \*\* : p<0.01). Note the fact that the majority of mitoses take place at the ventricular  
855 surface in the control condition while TBC1D3 brains display a shift towards more abventricular  
856 mitoses (arrowheads in D'). Scale bars (B,B',D,D') = 50 µm.

857 **Figure 2: Lis1 inactivation in forebrain neural progenitors severely impairs neocortical**  
858 **development in the KO, while heterozygotes show no major effects. A)** Schematic view of the  
859 protocol used: *Lis1*<sup>fl/+</sup> Emx1-Cre<sup>+/-Cre</sup> mice were crossed with *Lis1*<sup>fl/fl</sup> to produce WT (*Lis1*<sup>fl/fl</sup>), HET

860 (*Lis1*<sup>fl/+</sup> Emx1-Cre<sup>+Cre</sup>) and KO (*Lis1*<sup>fl/fl</sup> Emx1-Cre<sup>+Cre</sup>) animals. **B**) Nissl staining of *Lis1* WT, HET  
861 and KO P0 brain slices. HET brains show no macroscopic differences compared to WT animals. The  
862 cortex and medial areas in KO brains appear severely affected (absence of cortex and corpus  
863 callosum). **C**) Tbr1 immunohistochemistry (red) at E16.5 in WT and HET mouse brains to label deep-  
864 layer neurons. Nuclei counterstained with Hoechst dye. White squares display typical ROIs used for  
865 quantification of cell number. **D**) Quantification of cortical thickness (indicated by red arrows in A, 3  
866 animals per condition, one-way ANOVA, \*\* : p<0.01) showing no differences between WT and HET  
867 mice, and a large reduction in KO mice. **E**) Quantification of the number of Tbr1 cells per ROI (3 x 50  
868 μm slices per brain, 3 animals per condition, *t*-Test). No significant difference was observed between  
869 the genotypes. Scale bars (B) = 600 μm, (C) = 50 μm.

870 **Figure 3: *Lis1* depletion does not allow the generation of cycling bRG-like cells in the IZ in the**  
871 **presence of TBC1D3.** **A**) Schematic view of the protocol used: embryos from *Lis1*<sup>fl/fl</sup> females crossed  
872 with Emx1-Cre<sup>+Cre</sup> males were electroporated at E14.5 and sacrificed at E16.5. **B - E')** Pax6 (blue) and  
873 Ki67 (green) immunohistochemistry in E16.5 WT (B, B', D, D') and HET (C, C', E, E') mouse brains  
874 after electroporation of pCS2-cMyc-Control + tdTomato (Control, B, B', C, C') and pCS2-cMyc-  
875 TBC1D3 + tdTomato (TBC1D3, D, D', E, E') plasmids. tdTomato alone and the merge of tdTomato,  
876 Pax6 and Ki67 staining are shown for each condition. **F - I**) Proportion of Pax6+ tdTomato+ /  
877 tdTomato+ (F), Ki67+ tdTomato+ / tdTomato+ (G), Pax6+ Ki67+ tdTomato+ / tdTomato+ (H) and  
878 Pax6+ Ki67+ tdTomato / Pax6+ tdTomato+ (I) cells in WT and HET brains electroporated with  
879 control or TBC1D3 plasmids. Results are presented as percentages across the cortical wall ('Total') or  
880 within each cortical region (3 x 50 μm slices per brain, n=4 animals per condition, 2 Way ANOVA  
881 with Tukey *post hoc*, \*: p<0,05). Note TBC1D3 significantly increases Pax6+ and Pax6+Ki67+  
882 proportions in the IZ, and this increase is prevented by *Lis1* depletion. Scale bars (B-E') = 50 μm.

883 **Figure 4: *Lis1* depletion has no effect on intermediate progenitors upon TBC1D3**  
884 **overexpression.** **A - D')** Tbr2 (blue) and Ki67 (green) immunohistochemistry in E16.5 WT (A, A',  
885 C, C') and HET (B, B', D, D') mouse brains after electroporation at E14.5 of pCS2-cMyc-Control +  
886 tdTomato (Control, A, A', B, B') and pCS2-cMyc-TBC1D3 + tdTomato (TBC1D3, C, C', D, D')

887 plasmids. tdTomato alone and the merge of tdTomato, Ki67 and Ki67 staining are shown. **E - G)**  
888 Proportion of Tbr2+ tdTomato / tdTomato+ (E), Tbr2+ Ki67+ tdTomato+ / tdTomato+ (F), Tbr2+  
889 Ki67+ tdTomato+ / Tbr2+ tdTomato+ (G) in WT and HET brains electroporated with control or  
890 TBC1D3 plasmids. Results are represented as percentages across the cortical wall ('Total') or within  
891 each cortical region (3 x 50  $\mu$ m slices per brain, n=5-8 animals per condition for Tbr2+ tdTomato+ /  
892 tdTomato analysis, n= 3 animals per condition for other analyses, 2 Way ANOVA with Tukey *post*  
893 *hoc*). Scale bars (A-D') = 50  $\mu$ m.

894 **Figure 5: Lis1 depletion perturbs N-Cadherin expression at the ventricular surface.** A) N-  
895 Cadherin immunohistochemistry in E16.5 WT and HET mouse brains after electroporation at E14.5  
896 with pCS2-cMyc-Control + tdTomato (Control) and pCS2-cMyc-TBC1D3 + tdTomato (TBC1D3)  
897 plasmids. Panel shows N-Cadherin (N-Cad), tdTomato (Tomato), and merge panels for each  
898 condition. **B)** Quantification procedure for N-Cadherin fluorescence: 10  $\mu$ m lines contacting  
899 perpendicularly to the ventricular surface were drawn on ImageJ, and fluorescence intensity was  
900 measured every micron along the lines. Quantification was performed at non-junctions sites (in the  
901 middle of cells, line 1), at the cell adhesion sites (in between cells, line 2), and for the total by  
902 combining both. **C - E)** Quantification of N-Cadherin total (C), "*non-junction*" (D) and "*junction*" (E)  
903 fluorescence intensity (arbitrary units) at the ventricular surface every  $\mu$ m along a 10  $\mu$ m line  
904 perpendicular to the ventricular surface. The extremity of the ventricular surface is marked as 0 on the  
905 X axis. (3 x 50  $\mu$ m slices per brain, 3-4 animals per condition, 2-way ANOVA for repeated measures  
906 with Bonferoni *post hoc*, \*, \*\*, \*\*\* : p<0,05, p<0.01, p<0.001 respectively between TBC1D3 WT and  
907 TBC1D3 HET, §, §§, §§§ : p<0,05, p<0.01, p<0.001 respectively between Control HET and TBC1D3  
908 WT,  $\aleph$  : p<0.05 between Control WT and TBC1D3 HET). Scale bars (A) = 20  $\mu$ m, (B) = 5  $\mu$ m.

909 **Figure 6: Both Lis1 mutation and TBC1D3 increase abventricular mitoses but only Lis1**  
910 **dramatically perturbs mitotic spindle orientations.** A) PH3 immunohistochemistry (blue) in E16.5  
911 WT and HET mouse brains after electroporation at E14.5 with pCS2-cMyc-Control + tdTomato  
912 (Control) and pCS2-cMyc-TBC1D3 + tdTomato (TBC1D3) plasmids. **B)** Proportion of PH3+  
913 tdTomato+ / tdTomato+ in each cortical region and in the whole cortex ('Total') per ROI in WT or

914 HET mice electroporated with Control or TBC1D3 plasmids (3 x 50  $\mu$ m slices per brain, 7 animals per  
915 condition, 2-way ANOVA with Bonferoni *post hoc*). **C)** Distribution of ventricular mitoses versus  
916 abventricular mitoses (3 x 50  $\mu$ m slices per brain, 7 animals per condition, 2-way ANOVA with  
917 Bonferoni *post hoc*, \* :  $p > 0,05$ ). Note that the majority of mitoses take place at the ventricular surface  
918 in the control WT condition, while control HET, TBC1D3 WT and TBC1D3 HET brains display a  
919 significant shift towards abventricular mitoses. **D)** Distribution of mitotic spindle angles in  
920 electroporated cells dividing at the ventricular surface. Note wider variability for *Lis1* HET conditions  
921 with resulting lower angle mean. **E)** Mitotic spindle angles (categorized in vertical (90°-61°), oblique  
922 (60°-31°) and horizontal (30°-1°)) in electroporated cells dividing at the ventricular surface. Example  
923 of aRG mitoses for which the mitotic spindle angles were measured. **F)** Note that *Lis1* HET depletion  
924 dysregulates mitotic spindle angles by generating horizontal angles at the expense of vertical and  
925 oblique both in control and TBC1D3 conditions. For D,F 8-16 cells in 3 brain slices of n=6-8 animals  
926 per condition. Scale bars (A) = 50  $\mu$ m, (E) = 6  $\mu$ m.

927 **Supplementary Figure 1. Double labeling tdTomato and cMyc immunohistochemistry.** The vast  
928 majority of cells co-express tdTomato and cMyc in all three regions (VZ, SVZ and IZ) in E16.5 WT  
929 mice after brain IUE at E14.5 with tdTomato + pCS2-cMyc-TBC1D3. Scale bar = 100  $\mu$ m.

930 **Supplementary Figure 2. Pattern of Cre recombination in the *Emx1-Cre* x RCE mouse brain at**  
931 **E16.5.** EGFP labeling in coronal section of a E16.5 mouse brain from control (A) and *Emx1-ires-Cre*;  
932 *Rosa26-EGFP* RCE/RCE genotype mice (B). The Cre recombination occurs only in the pallium  
933 (higher magnification in C) and not the subpallium. Scale bars (A-B) = 340  $\mu$ m, (C) = 226  $\mu$ m.

934 **Supplementary Figure 3. *Lis1* depletion in the heterozygous state with TBC1D3 expression does**  
935 **not lead to increased cell death.** **A)** Activated Caspase 3 immunohistochemistry (aCas3, blue) in  
936 E16.5 WT and HET mice after IUE at E14.5 with tdTomato + pCS2-cMyc-Control (Control) and  
937 tdTomato + pCS2-cMyc-TBC1D3 (TBC1D3) electroporated brains. **B)** Quantification of aCas3  
938 clusters per ROI in Control WT and HET, and TBC1D3 WT and HET animals. No significant  
939 differences were observed, but there were tendencies for an increase when *Lis1* is depleted and for  
940 when TBC1D3 is expressed. Scale bars (A) = 50  $\mu$ m.

941 **Supplementary Figure 4. Higher magnifications of Pax6, Ki67 immunohistochemistry in 4**  
942 **conditions studied.** Pax6 (blue) and Ki67 (green) immunohistochemistry in E16.5 WT and HET  
943 mouse brains after electroporation of pCS2-cMyc-Control + tdTomato (Control) and pCS2-cMyc-  
944 TBC1D3 + tdTomato (TBC1D3) plasmids. All channels alone and the merge of tdTomato, Pax6 and  
945 Ki67 staining are shown for each condition. Scale bar = 50  $\mu$ m.

946 **Supplementary Figure 5. Expression of Pax6 and Ki67 in WT and HET E16 brains to identify**  
947 **cycling Pax6+ cells. A)** Representative images from non-electroporated WT and HET E16 brains  
948 sections probed with anti-Ki67 (green) and anti-Pax6 (red) antibodies. Scale bar = 50  $\mu$ m. **B)**  
949 Proportion of Ki67+/Pax6+ cells in each region of non-electroporated WT and HET brains. n=3, *P*-  
950 values were calculated using ANOVA, mean  $\pm$  SD. There is no significant difference in cell number  
951 and position between the two conditions in all three each regions examined. Combined and total  
952 number also does not differ.

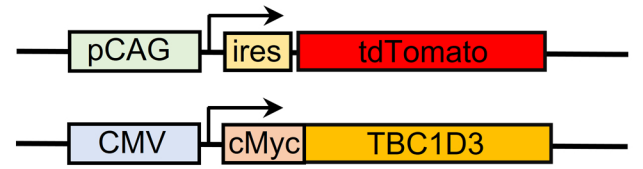
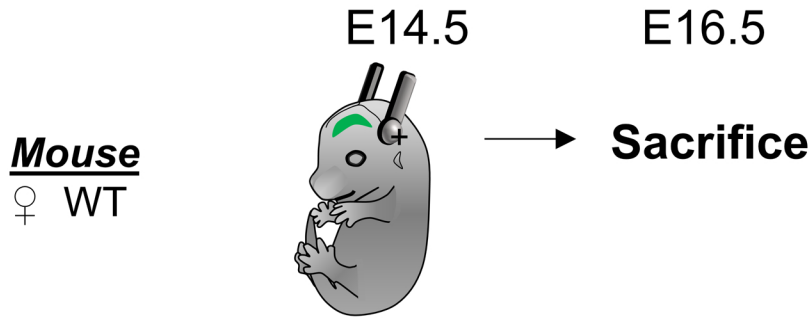
953 **Supplementary Figure 6. *En-face* view imaging of F-actin organization in the ventricular zone in**  
954 **4 conditions.** Representative images from tdTomato (red) and F-actin (green) Phalloidin-488 *en-face*  
955 VZ staining in E16.5 WT and HET mouse brains after electroporation of pCS2-cMyc-Control +  
956 tdTomato (Control) and pCS2-cMyc-TBC1D3 + tdTomato (TBC1D3) plasmids. Phalloidin-488  
957 revealed the presence of F-actin honeycomb structures around TdTomato+ cells (arrows) and  
958 TdTomato- cells as well. There is no obvious difference in F-actin organization in the 4 conditions.  
959 Scale bar = 18  $\mu$ m.

960 **Supplementary Figure 7. Higher magnifications of tdTomato electroporated cells in WT and**  
961 **HET conditions.** Representative images from tdTomato electroporated cells (red) from 3 consecutive  
962 sections (a-c) from WT and HET E16.5 brains after Hoechst staining (blue). In WT and HET,  
963 vertically oriented cells are present in the VZ (arrows), as well as more oblique soma in the HET  
964 (arrowheads). In both genotypes, numerous tdTomato+ cells contact the ventricle. Scale bar = 24  $\mu$ m.

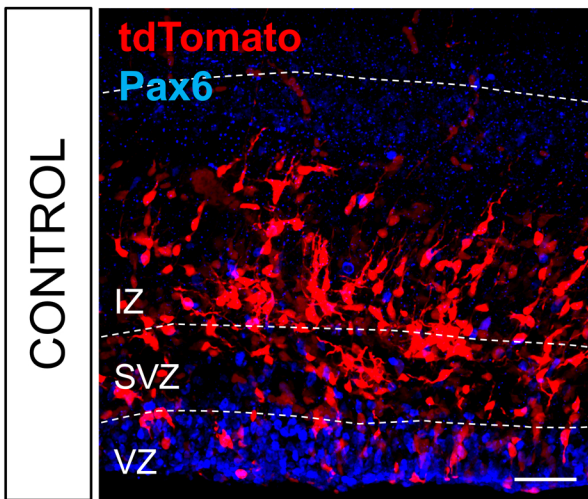
965

# FIGURE 1

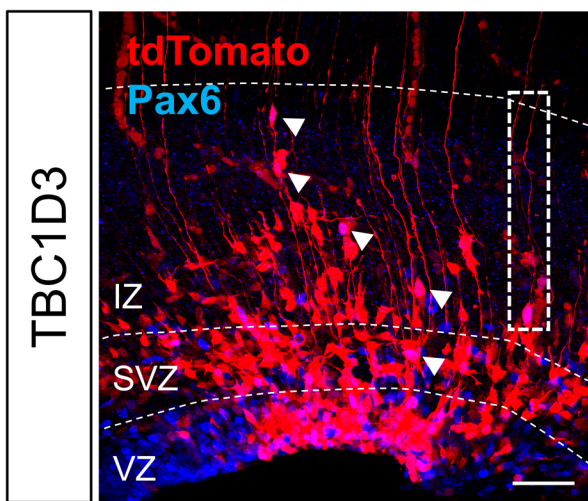
A



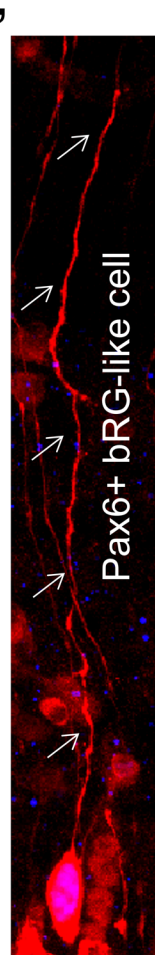
B



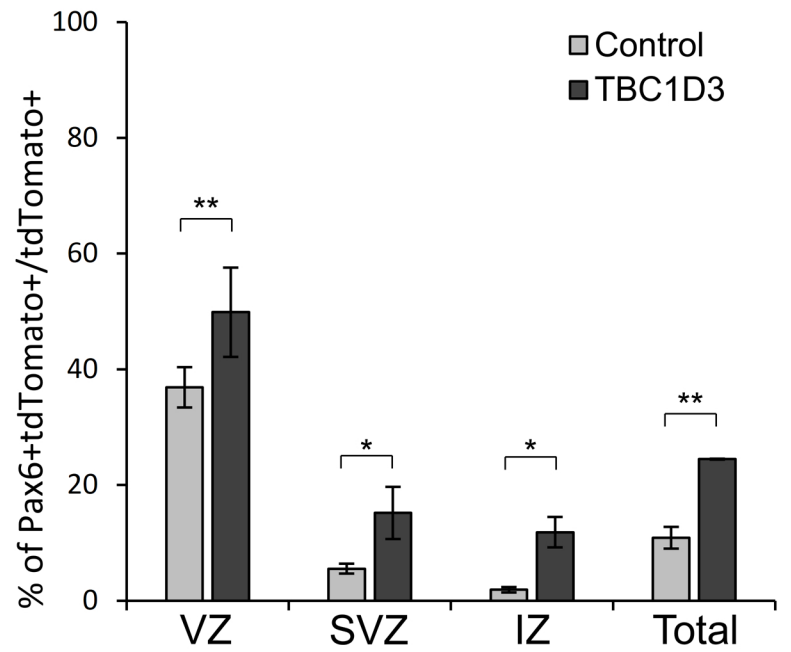
B'



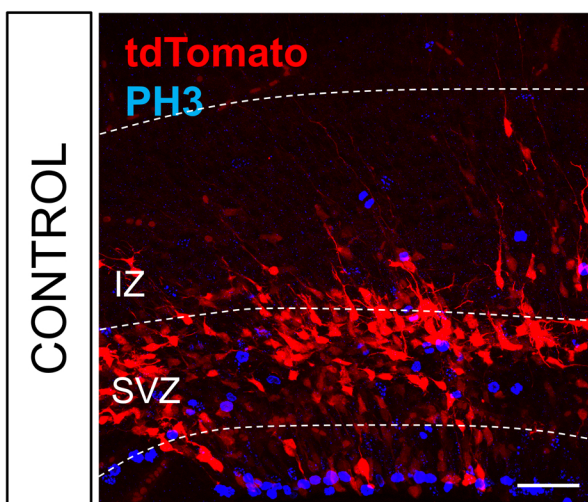
B''



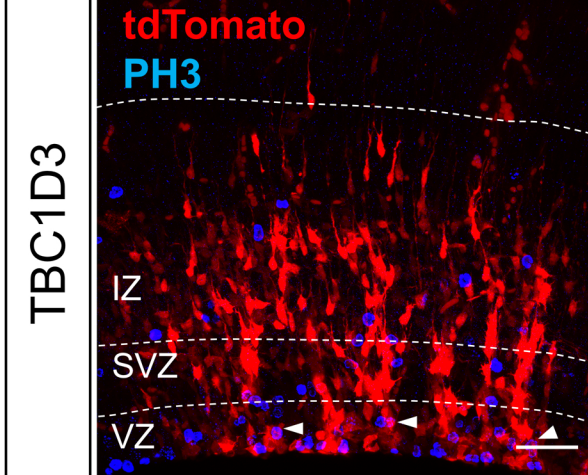
C



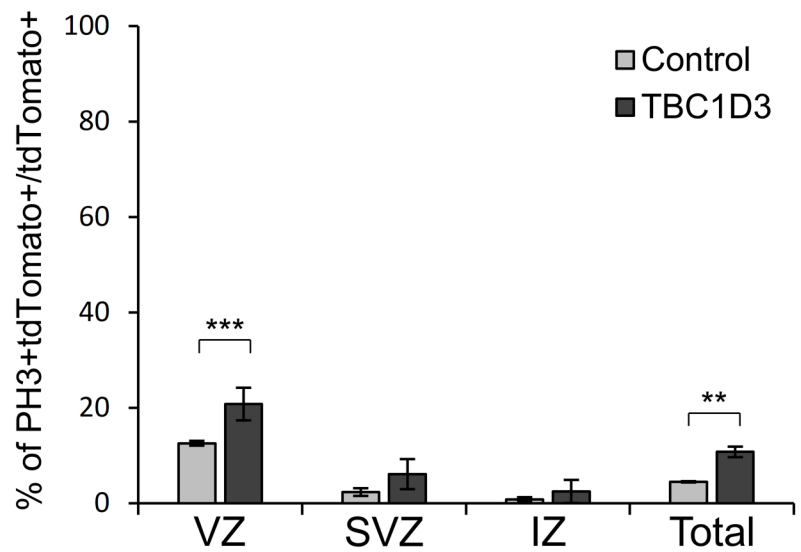
D



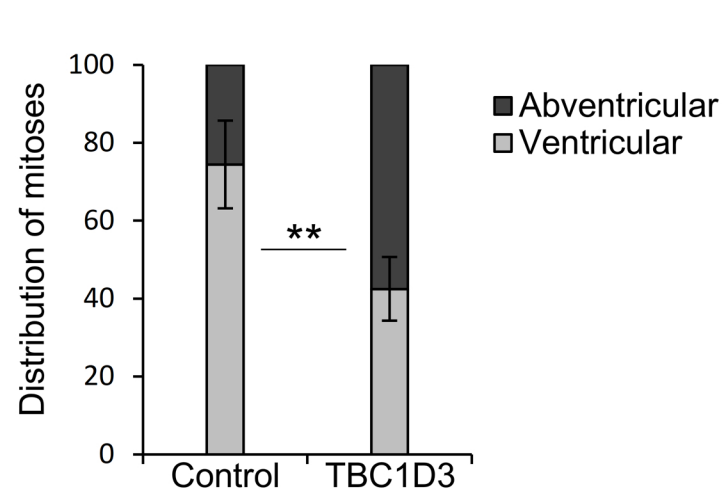
D'



E



F


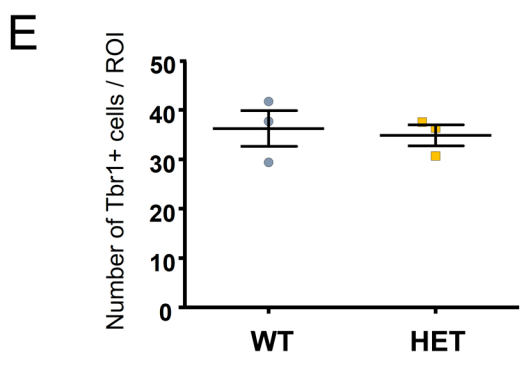
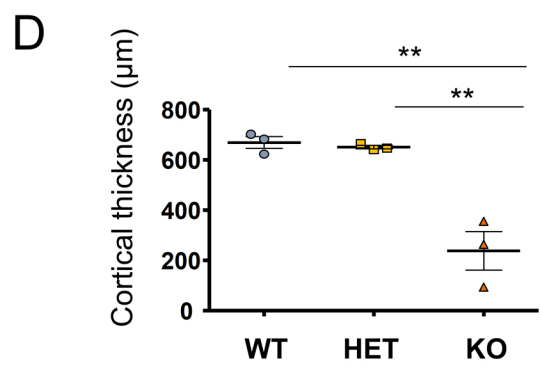
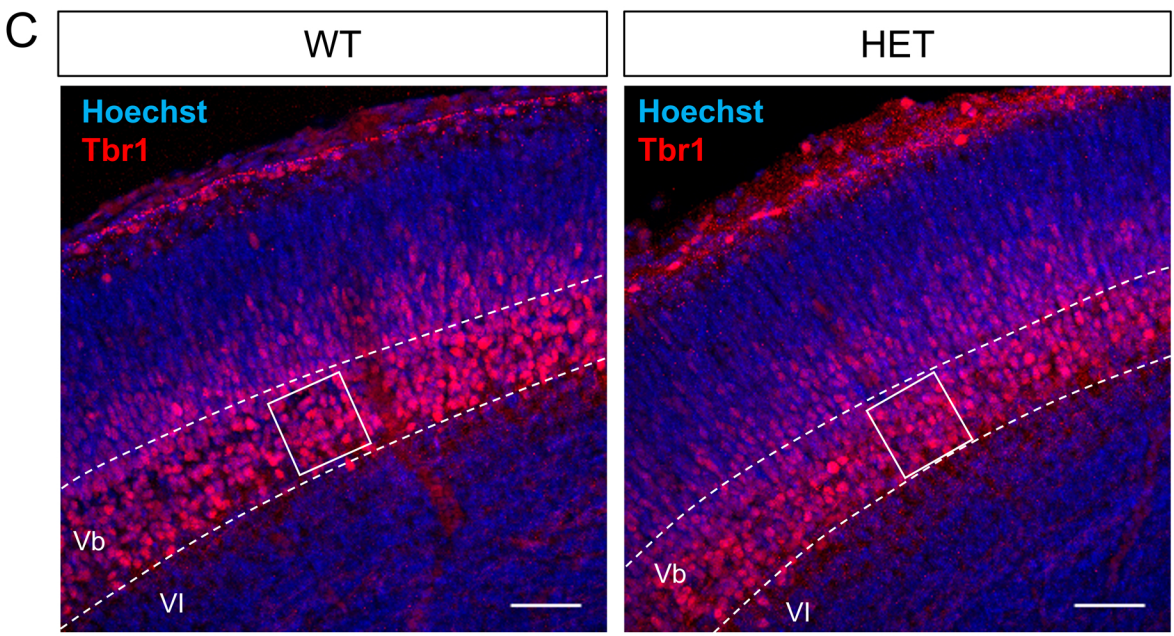
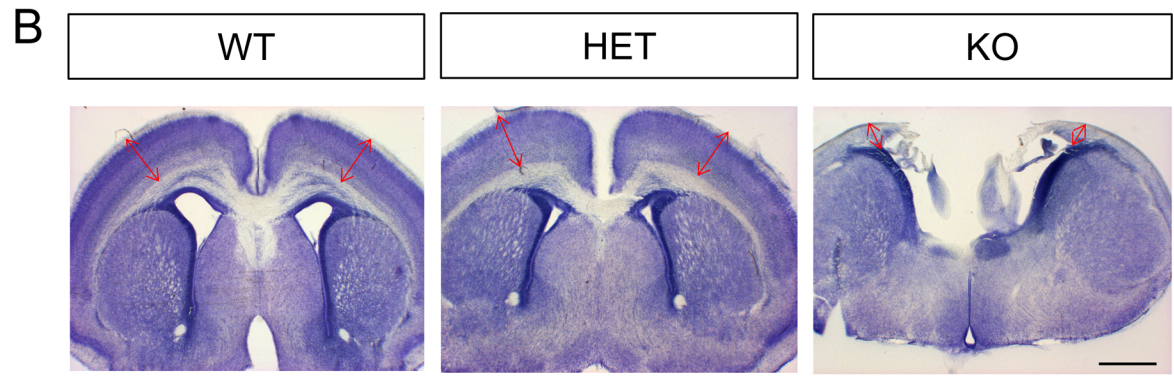




# FIGURE 2

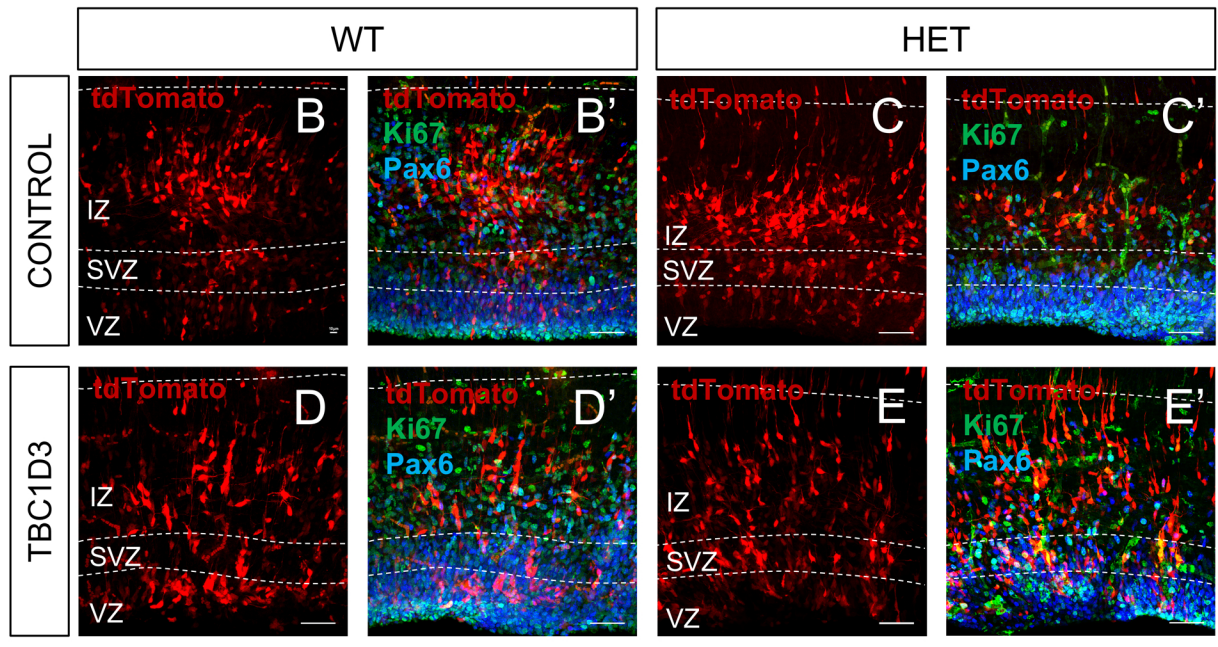
**A** E16.5 & P0

**Mouse**  
 ♀  $Lis1^{fl/fl}$   
 crossed with  
 ♂  $Lis1^{fl/+} Emx1-Cre^{+/Cre}$

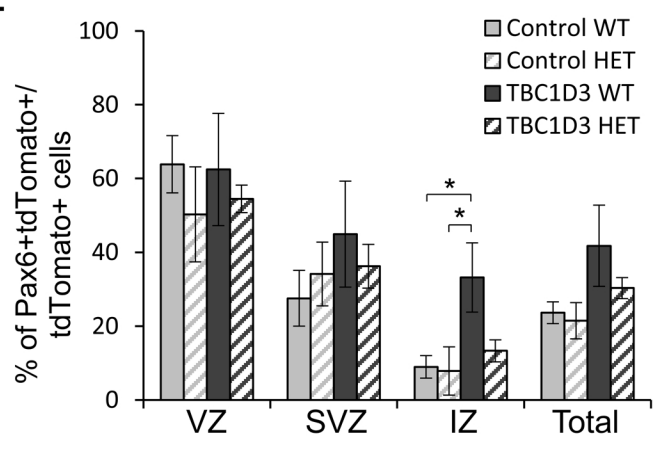



# FIGURE 3

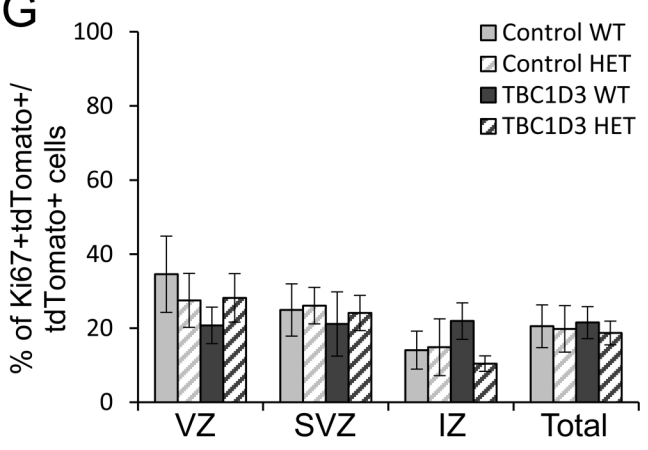
A



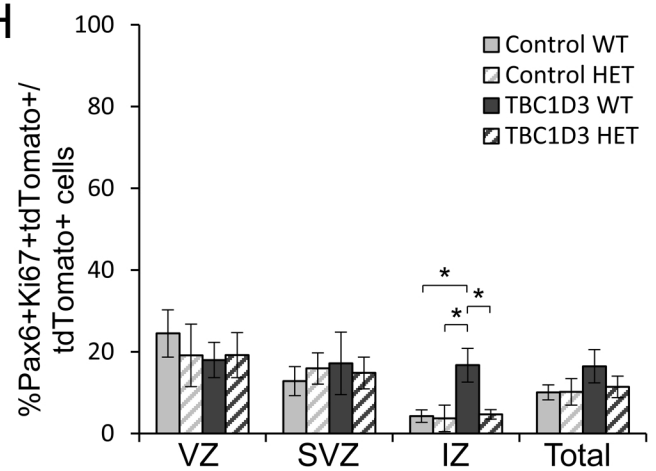
F



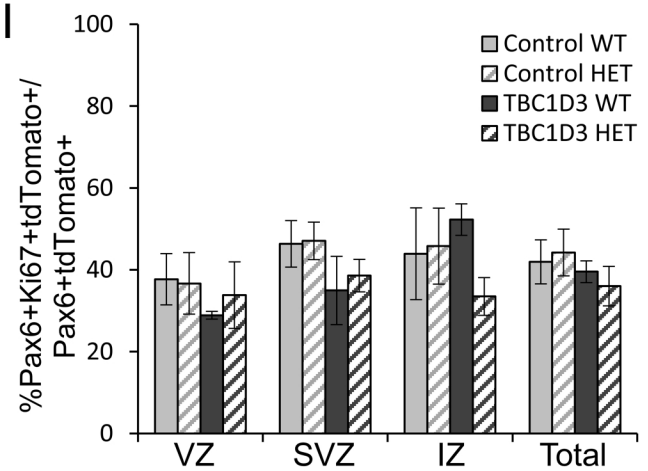
G



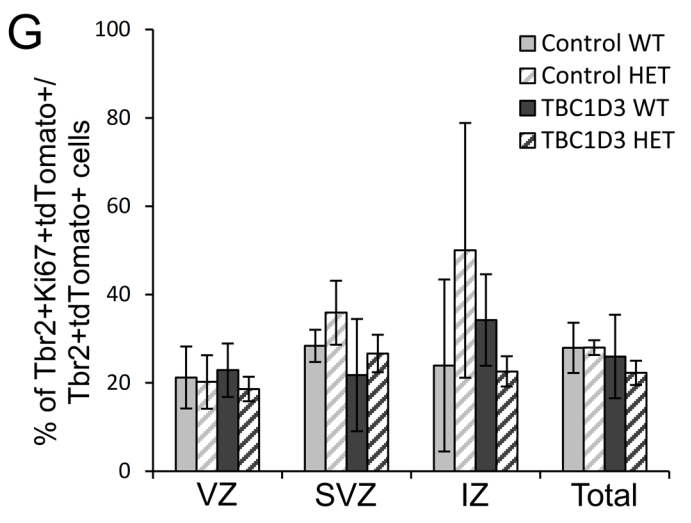
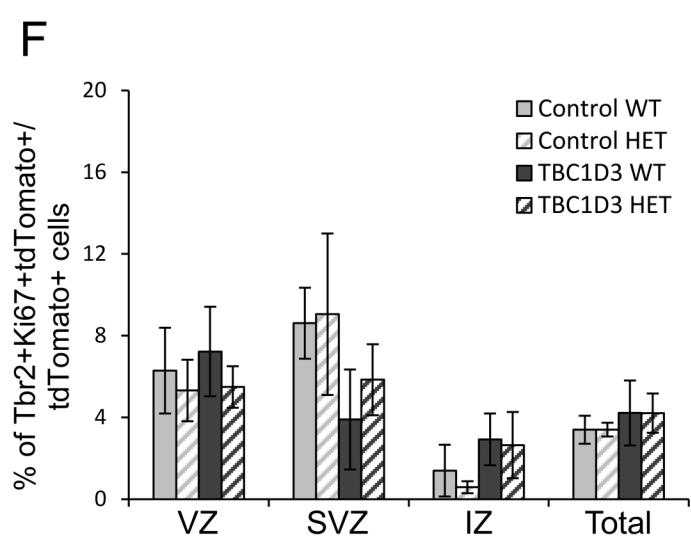
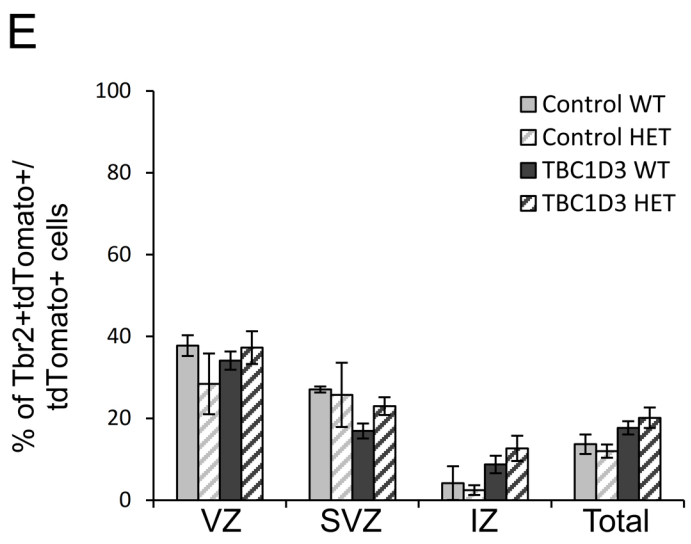
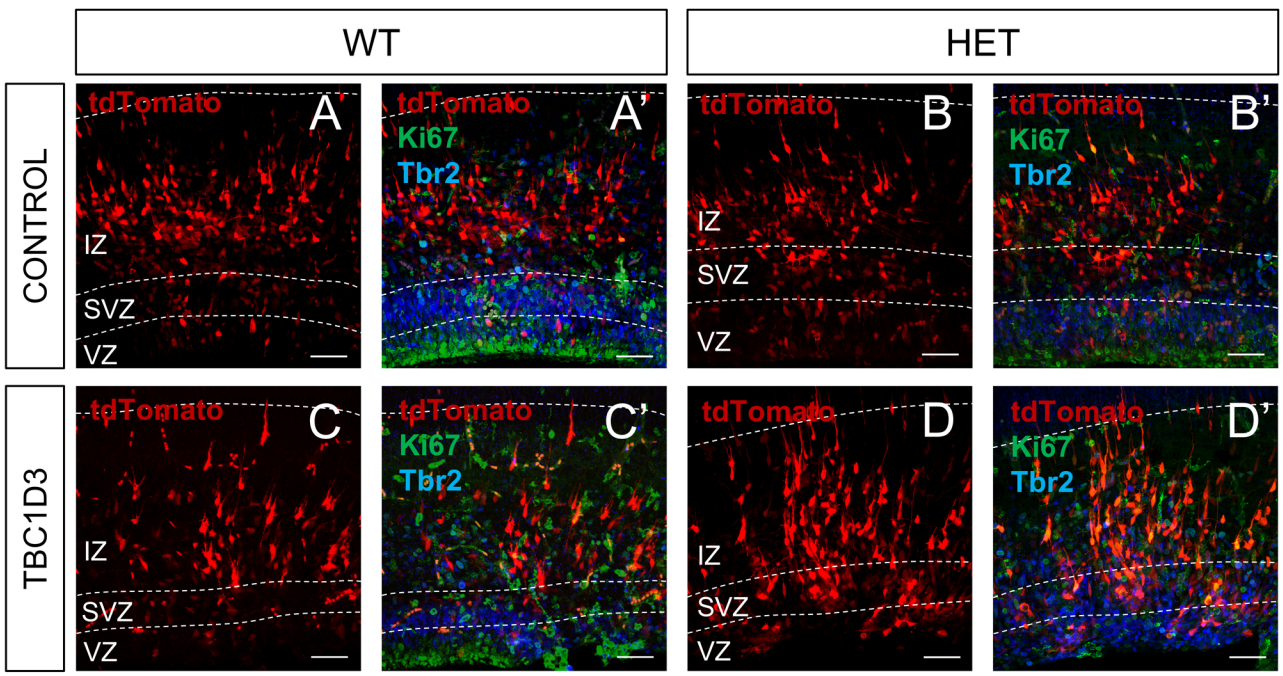
H



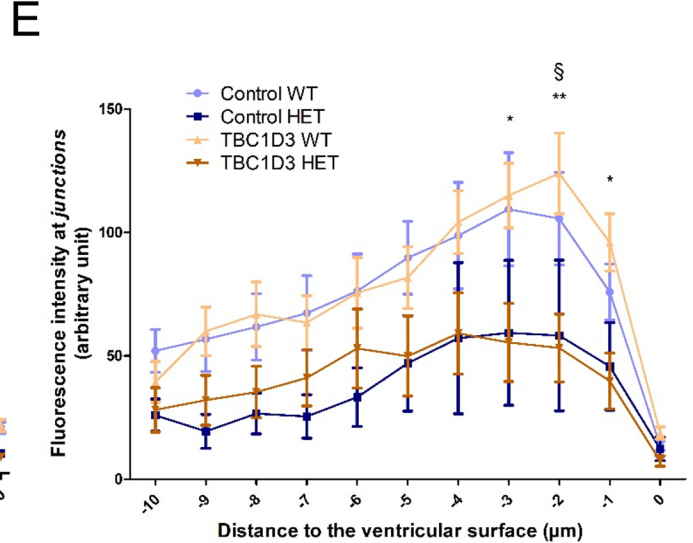
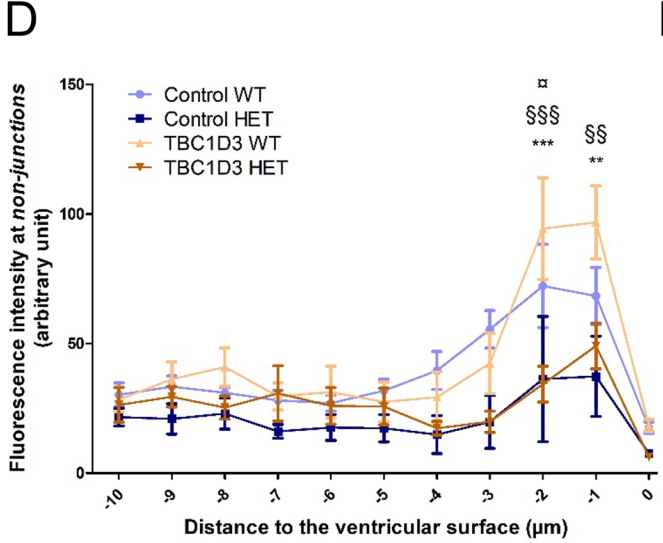
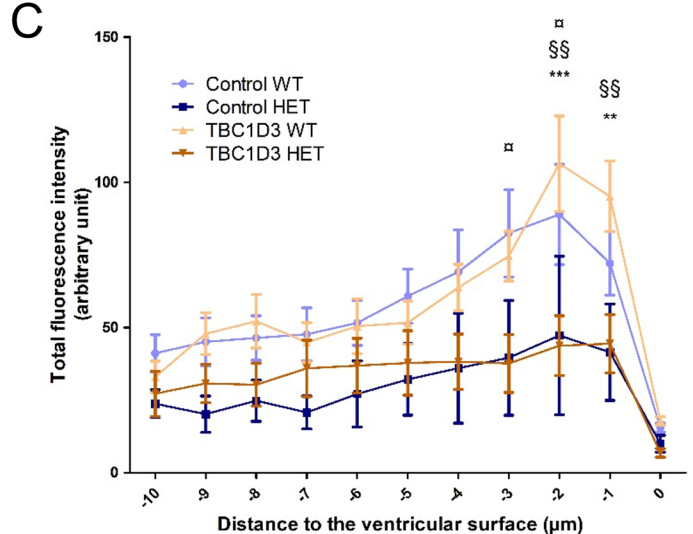
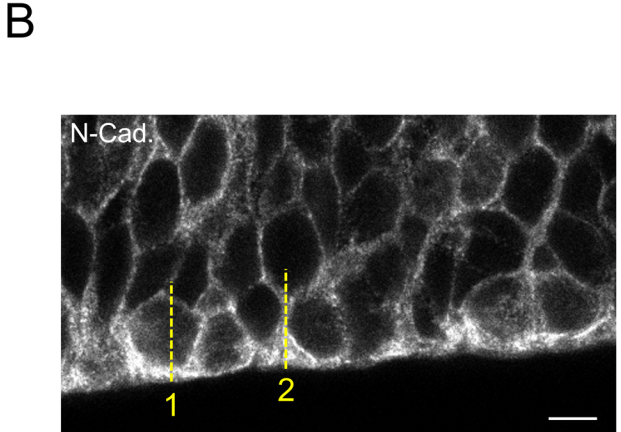
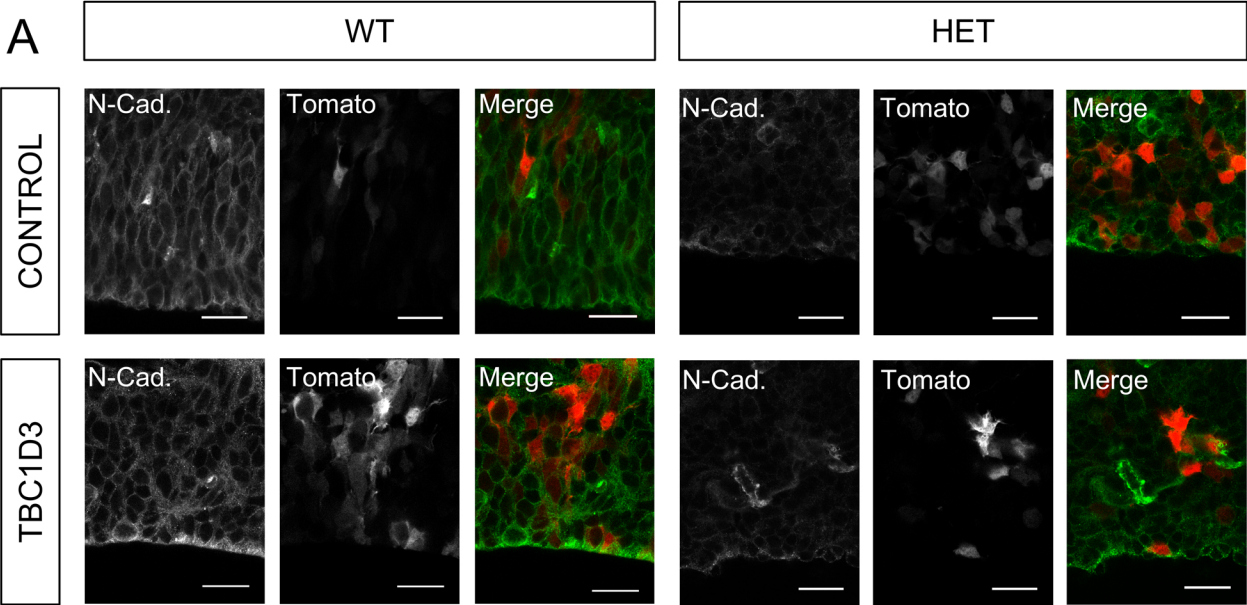
I



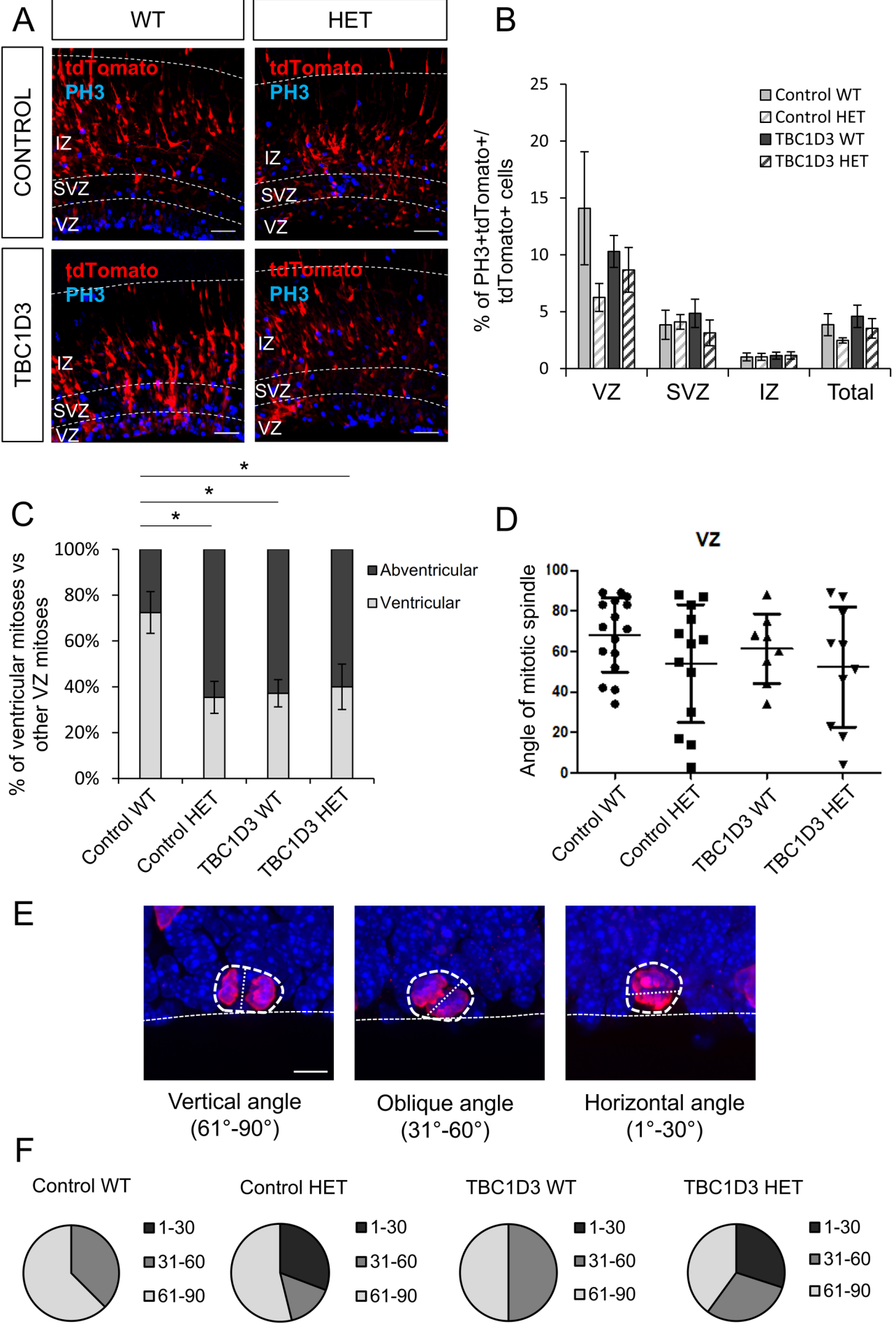
**FIGURE 4**



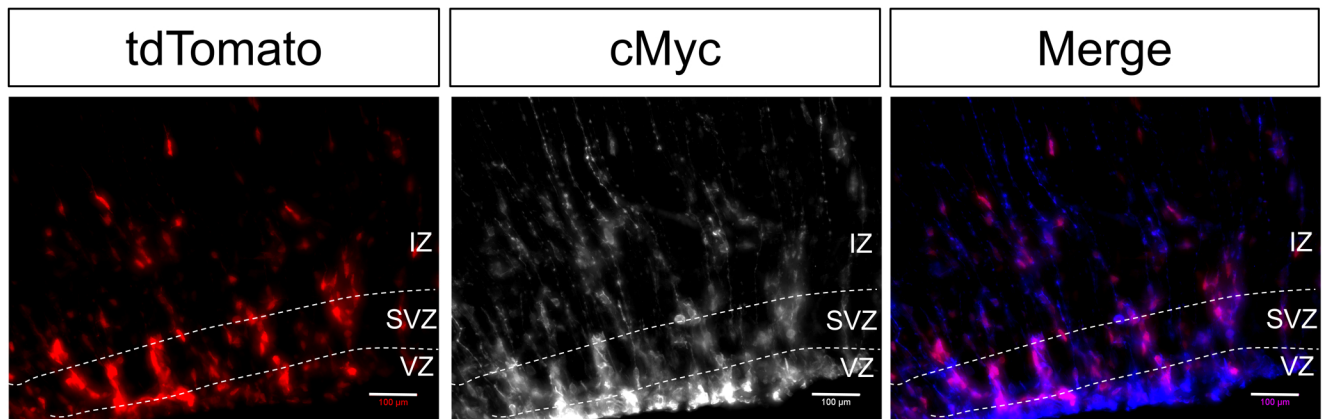
# FIGURE 5



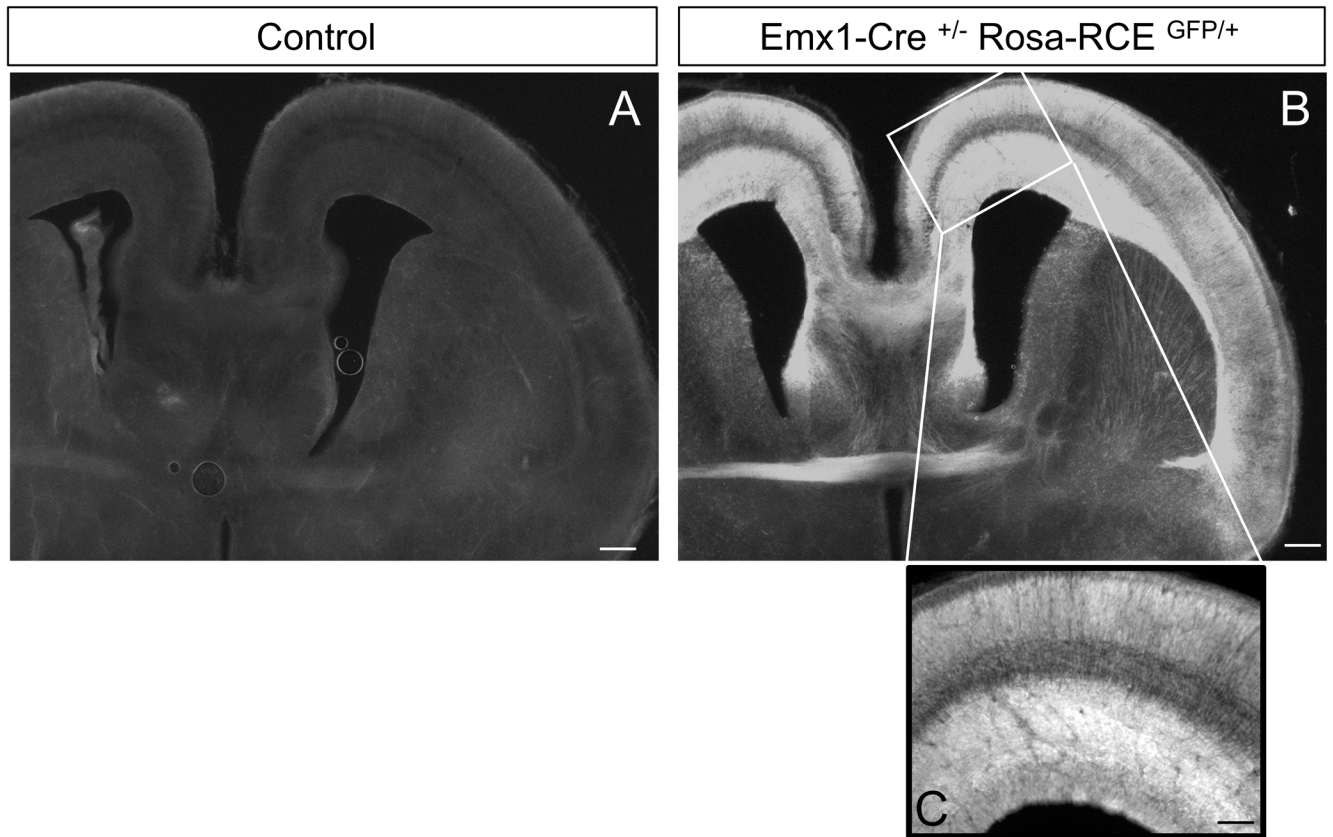
**FIGURE 6**



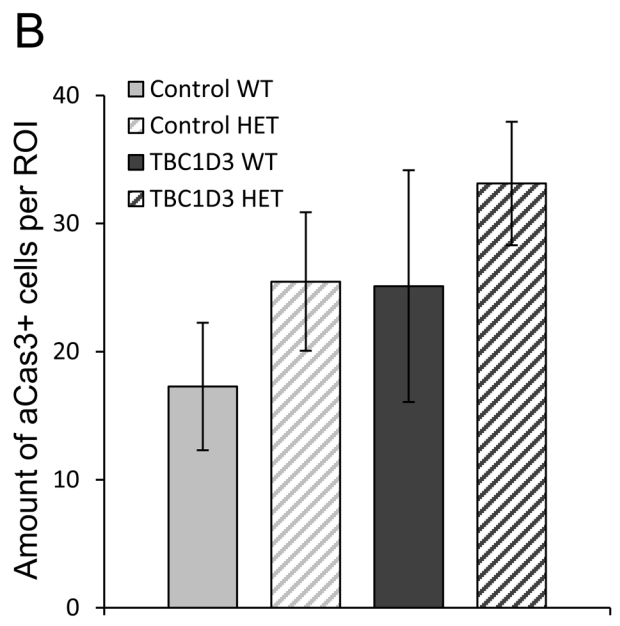
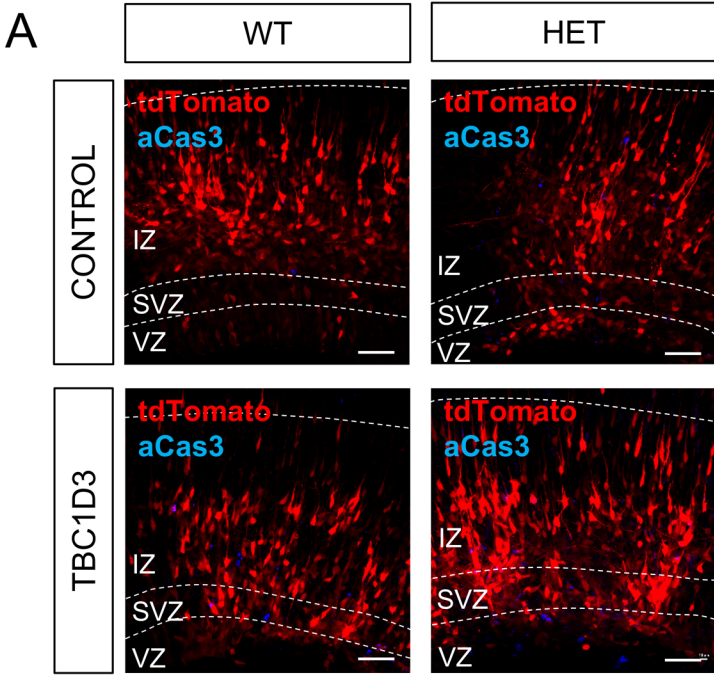
# Supplementary FIGURE 1



# Supplementary FIGURE 2

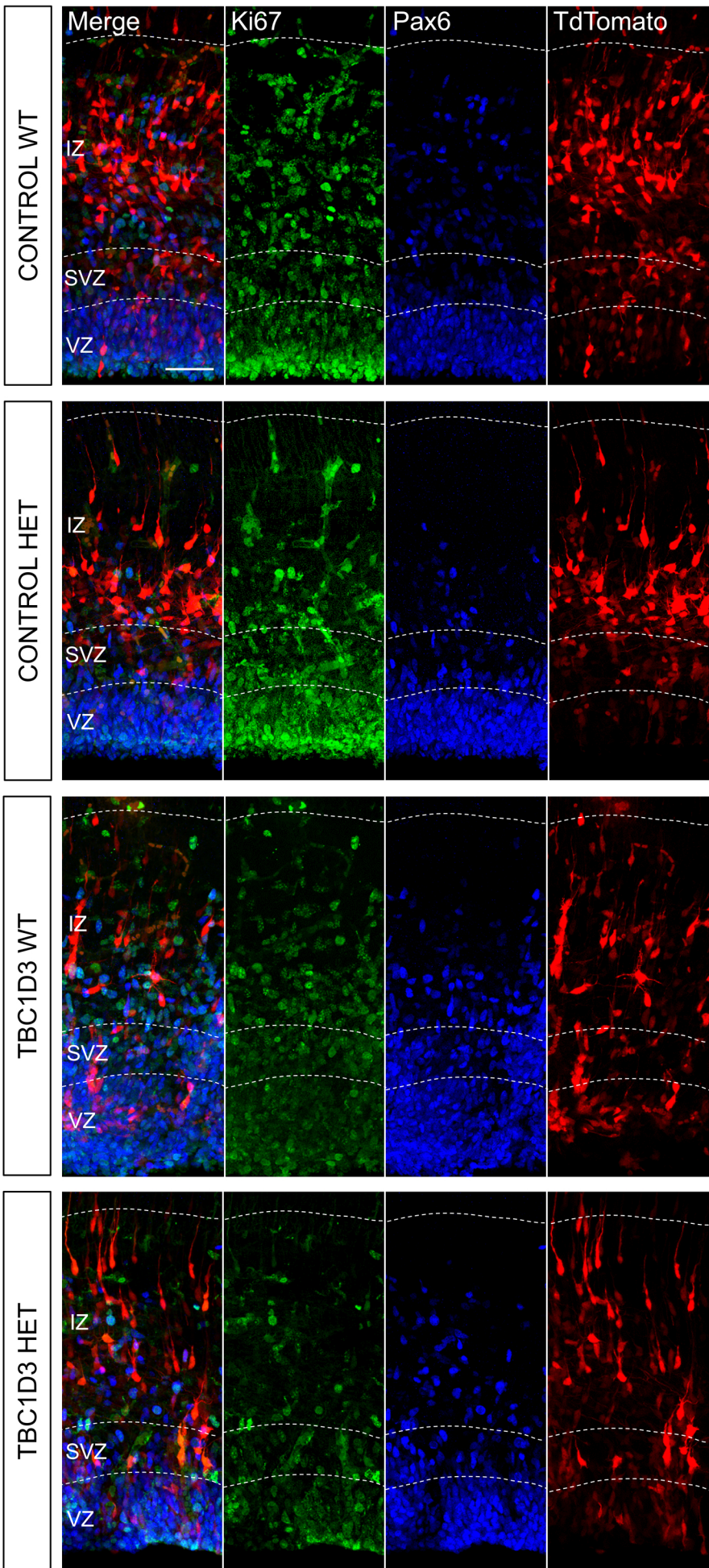


# Supplementary FIGURE 3

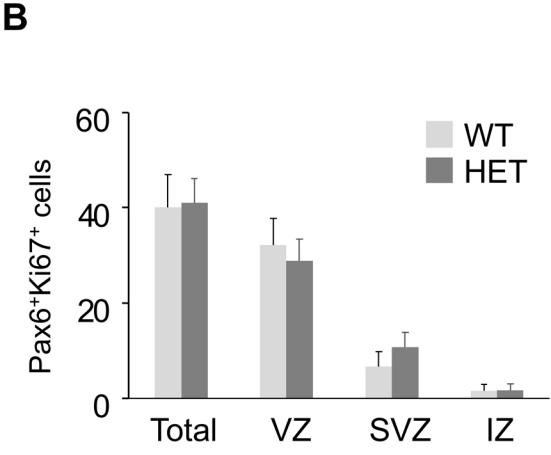
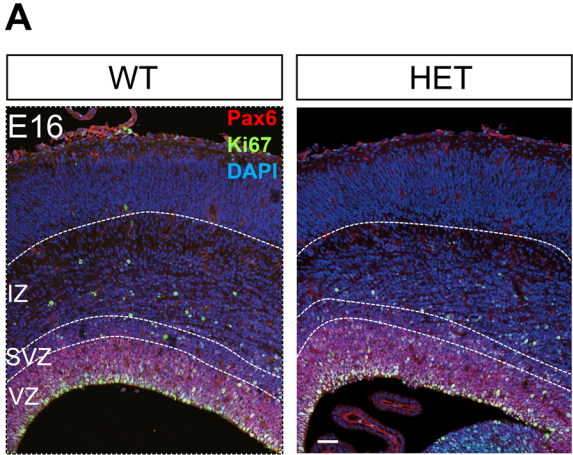




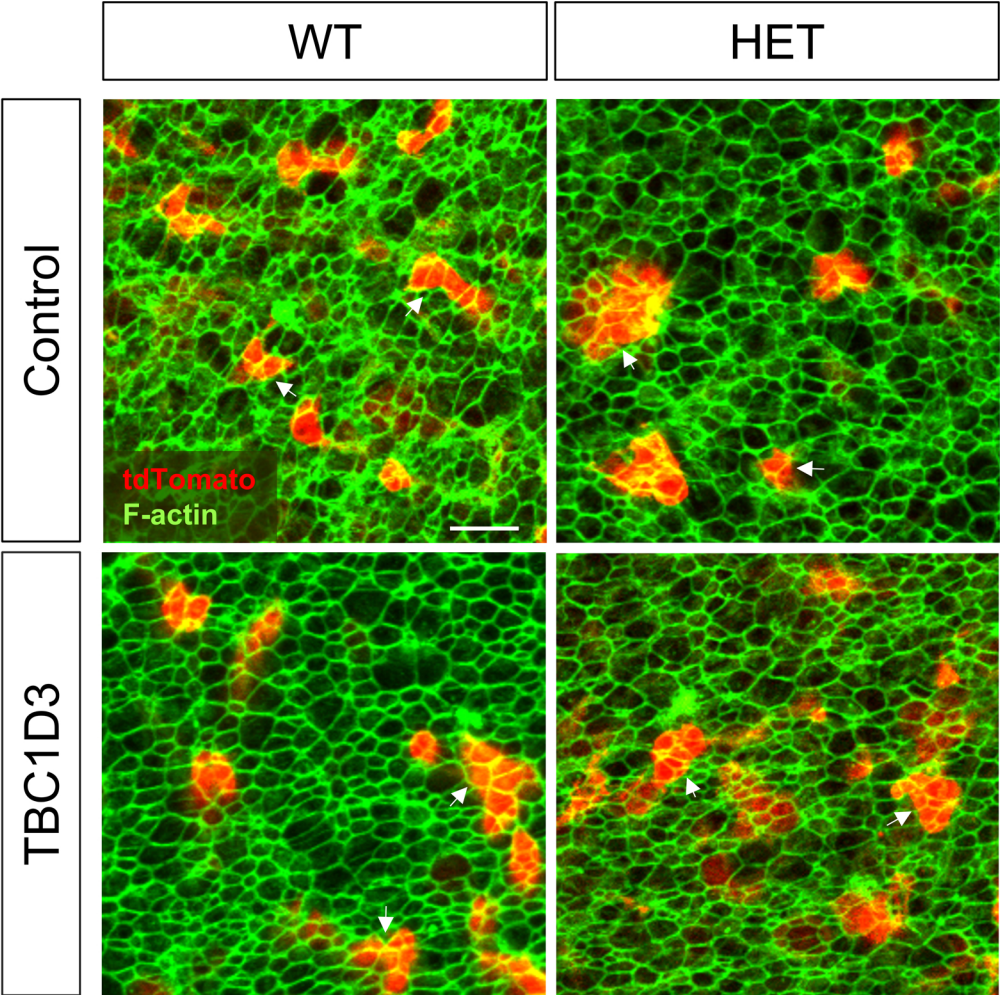
# Supplementary FIGURE 4



# Supplementary FIGURE 5



Supplementary FIGURE 6



# Supplementary FIGURE 7

